

## Gamma-ray observations of the Orion Molecular Clouds with the *Fermi* Large Area Telescope

M. Ackermann<sup>1</sup>, M. Ajello<sup>2</sup>, A. Allafort<sup>2</sup>, E. Antolini<sup>3,4</sup>, L. Baldini<sup>5</sup>, J. Ballet<sup>6</sup>, G. Barbiellini<sup>7,8</sup>, D. Bastieri<sup>9,10</sup>, K. Bechtol<sup>2</sup>, R. Bellazzini<sup>5</sup>, B. Berenji<sup>2</sup>, R. D. Blandford<sup>2</sup>, E. D. Bloom<sup>2</sup>, E. Bonamente<sup>3,4</sup>, A. W. Borgland<sup>2</sup>, E. Bottacini<sup>2</sup>, T. J. Brandt<sup>11,12</sup>, J. Bregeon<sup>5</sup>, M. Brigida<sup>13,14</sup>, P. Bruel<sup>15</sup>, R. Buehler<sup>2</sup>, S. Buson<sup>9,10</sup>, G. A. Caliandro<sup>16</sup>, R. A. Cameron<sup>2</sup>, P. A. Caraveo<sup>17</sup>, C. Cecchi<sup>3,4</sup>, A. Chekhtman<sup>18</sup>, J. Chiang<sup>2</sup>, S. Ciprini<sup>19,4</sup>, R. Claus<sup>2</sup>, J. Cohen-Tanugi<sup>20</sup>, J. Conrad<sup>21,22,23</sup>, F. D'Ammando<sup>3,24,25</sup>, A. de Angelis<sup>26</sup>, F. de Palma<sup>13,14</sup>, C. D. Dermer<sup>27</sup>, E. do Couto e Silva<sup>2</sup>, P. S. Drell<sup>2</sup>, A. Drlica-Wagner<sup>2</sup>, T. Enoto<sup>2</sup>, L. Falletti<sup>20</sup>, C. Favuzzi<sup>13,14</sup>, S. J. Fegan<sup>15</sup>, E. C. Ferrara<sup>28</sup>, W. B. Focke<sup>2</sup>, Y. Fukazawa<sup>29</sup>, Y. Fukui<sup>30</sup>, P. Fusco<sup>13,14</sup>, F. Gargano<sup>14</sup>, D. Gasparrini<sup>31</sup>, S. Germani<sup>3,4</sup>, N. Giglietto<sup>13,14</sup>, F. Giordano<sup>13,14</sup>, M. Giroletti<sup>32</sup>, T. Glanzman<sup>2</sup>, G. Godfrey<sup>2</sup>, S. Guiriec<sup>33</sup>, D. Hadasch<sup>16</sup>, Y. Hanabata<sup>29</sup>, A. K. Harding<sup>28</sup>, M. Hayashida<sup>2,34</sup>, K. Hayashi<sup>29</sup>, D. Horan<sup>15</sup>, X. Hou<sup>35</sup>, R. E. Hughes<sup>36</sup>, M. S. Jackson<sup>37,22</sup>, G. Jóhannesson<sup>38</sup>, A. S. Johnson<sup>2</sup>, T. Kamae<sup>2,39</sup>, H. Katagiri<sup>40</sup>, J. Kataoka<sup>41</sup>, M. Kerr<sup>2</sup>, J. Knödseder<sup>11,12</sup>, M. Kuss<sup>5</sup>, J. Lande<sup>2</sup>, S. Larsson<sup>21,22,42</sup>, S.-H. Lee<sup>43</sup>, F. Longo<sup>7,8</sup>, F. Loparco<sup>13,14</sup>, M. N. Lovellette<sup>27</sup>, P. Lubrano<sup>3,4</sup>, K. Makishima<sup>44</sup>, M. N. Mazziotta<sup>14</sup>, J. Mehault<sup>20</sup>, W. Mitthumsiri<sup>2</sup>, A. A. Moiseev<sup>45,46</sup>, C. Monte<sup>13,14</sup>, M. E. Monzani<sup>2</sup>, A. Morselli<sup>47</sup>, I. V. Moskalenko<sup>2</sup>, S. Murgia<sup>2</sup>, T. Nakamori<sup>41</sup>, M. Naumann-Godo<sup>6</sup>, S. Nishino<sup>29</sup>, J. P. Norris<sup>48</sup>, E. Nuss<sup>20</sup>, M. Ohno<sup>49</sup>, T. Ohsugi<sup>50</sup>, A. Okumura<sup>2,49,51</sup>, M. Orienti<sup>32</sup>, E. Orlando<sup>2</sup>, J. F. Ormes<sup>52</sup>, M. Ozaki<sup>49</sup>, D. Paneque<sup>53,2</sup>, J. H. Panetta<sup>2</sup>, D. Parent<sup>18</sup>, V. Pelassa<sup>33</sup>, M. Pesce-Rollins<sup>5</sup>, M. Pierbattista<sup>6</sup>, F. Piron<sup>20</sup>, G. Pivato<sup>10</sup>, T. A. Porter<sup>2,2</sup>, S. Rainò<sup>13,14</sup>, M. Razzano<sup>5,54</sup>, A. Reimer<sup>55,2</sup>, O. Reimer<sup>55,2</sup>, M. Roth<sup>56</sup>, H. F.-W. Sadrozinski<sup>54</sup>, C. Sgrò<sup>5</sup>, E. J. Siskind<sup>57</sup>, G. Spandre<sup>5</sup>, P. Spinelli<sup>13,14</sup>, A. W. Strong<sup>58</sup>, H. Takahashi<sup>50</sup>, T. Takahashi<sup>49</sup>, T. Tanaka<sup>2</sup>, J. G. Thayer<sup>2</sup>, J. B. Thayer<sup>2</sup>, O. Tibolla<sup>59</sup>, M. Tinivella<sup>5</sup>, D. F. Torres<sup>16,60</sup>, A. Tramacere<sup>2,61,62</sup>, E. Troja<sup>28,63</sup>, Y. Uchiyama<sup>2</sup>, T. L. Usher<sup>2</sup>, J. Vandenbroucke<sup>2</sup>, V. Vasileiou<sup>20</sup>, G. Vianello<sup>2,61</sup>, V. Vitale<sup>47,64</sup>, A. P. Waite<sup>2</sup>, P. Wang<sup>2</sup>, B. L. Winer<sup>36</sup>, K. S. Wood<sup>27</sup>, Z. Yang<sup>21,22</sup>, S. Zimmer<sup>21,22</sup>

- 
- <sup>1</sup>Deutsches Elektronen Synchrotron DESY, D-15738 Zeuthen, Germany
- <sup>2</sup>W. W. Hansen Experimental Physics Laboratory, Kavli Institute for Particle Astrophysics and Cosmology, Department of Physics and SLAC National Accelerator Laboratory, Stanford University, Stanford, CA 94305, USA
- <sup>3</sup>Istituto Nazionale di Fisica Nucleare, Sezione di Perugia, I-06123 Perugia, Italy
- <sup>4</sup>Dipartimento di Fisica, Università degli Studi di Perugia, I-06123 Perugia, Italy
- <sup>5</sup>Istituto Nazionale di Fisica Nucleare, Sezione di Pisa, I-56127 Pisa, Italy
- <sup>6</sup>Laboratoire AIM, CEA-IRFU/CNRS/Université Paris Diderot, Service d'Astrophysique, CEA Saclay, 91191 Gif sur Yvette, France
- <sup>7</sup>Istituto Nazionale di Fisica Nucleare, Sezione di Trieste, I-34127 Trieste, Italy
- <sup>8</sup>Dipartimento di Fisica, Università di Trieste, I-34127 Trieste, Italy
- <sup>9</sup>Istituto Nazionale di Fisica Nucleare, Sezione di Padova, I-35131 Padova, Italy
- <sup>10</sup>Dipartimento di Fisica "G. Galilei", Università di Padova, I-35131 Padova, Italy
- <sup>11</sup>CNRS, IRAP, F-31028 Toulouse cedex 4, France
- <sup>12</sup>GAHEC, Université de Toulouse, UPS-OMP, IRAP, Toulouse, France
- <sup>13</sup>Dipartimento di Fisica "M. Merlin" dell'Università e del Politecnico di Bari, I-70126 Bari, Italy
- <sup>14</sup>Istituto Nazionale di Fisica Nucleare, Sezione di Bari, 70126 Bari, Italy
- <sup>15</sup>Laboratoire Leprince-Ringuet, École polytechnique, CNRS/IN2P3, Palaiseau, France
- <sup>16</sup>Institut de Ciències de l'Espai (IEEE-CSIC), Campus UAB, 08193 Barcelona, Spain
- <sup>17</sup>INAF-Istituto di Astrofisica Spaziale e Fisica Cosmica, I-20133 Milano, Italy
- <sup>18</sup>Center for Earth Observing and Space Research, College of Science, George Mason University, Fairfax, VA 22030, resident at Naval Research Laboratory, Washington, DC 20375, USA
- <sup>19</sup>ASI Science Data Center, I-00044 Frascati (Roma), Italy
- <sup>20</sup>Laboratoire Univers et Particules de Montpellier, Université Montpellier 2, CNRS/IN2P3, Montpellier, France
- <sup>21</sup>Department of Physics, Stockholm University, AlbaNova, SE-106 91 Stockholm, Sweden
- <sup>22</sup>The Oskar Klein Centre for Cosmoparticle Physics, AlbaNova, SE-106 91 Stockholm, Sweden
- <sup>23</sup>Royal Swedish Academy of Sciences Research Fellow, funded by a grant from the K. A. Wallenberg Foundation
- <sup>24</sup>IASF Palermo, 90146 Palermo, Italy
- <sup>25</sup>INAF-Istituto di Astrofisica Spaziale e Fisica Cosmica, I-00133 Roma, Italy
- <sup>26</sup>Dipartimento di Fisica, Università di Udine and Istituto Nazionale di Fisica Nucleare, Sezione di Trieste, Gruppo Collegato di Udine, I-33100 Udine, Italy
- <sup>27</sup>Space Science Division, Naval Research Laboratory, Washington, DC 20375-5352, USA
- <sup>28</sup>NASA Goddard Space Flight Center, Greenbelt, MD 20771, USA
- <sup>29</sup>Department of Physical Sciences, Hiroshima University, Higashi-Hiroshima, Hiroshima 739-8526, Japan
- <sup>30</sup>Department of Physics and Astrophysics, Nagoya University, Chikusa-ku Nagoya 464-8602, Japan

- 
- <sup>21</sup> Agenzia Spaziale Italiana (ASI) Science Data Center, I-00044 Frascati (Roma), Italy
- <sup>22</sup> INAF Istituto di Radioastronomia, 40129 Bologna, Italy
- <sup>23</sup> Center for Space Plasma and Aeronomic Research (CSPAR), University of Alabama in Huntsville, Huntsville, AL 35899, USA
- <sup>24</sup> Department of Astronomy, Graduate School of Science, Kyoto University, Sakyo-ku, Kyoto 606-8502, Japan
- <sup>25</sup> Centre d'Études Nucléaires de Bordeaux Gradignan, IN2P3/CNRS, Université Bordeaux 1, BP120, F-33175 Gradignan Cedex, France
- <sup>26</sup> Department of Physics, Center for Cosmology and Astro-Particle Physics, The Ohio State University, Columbus, OH 43210, USA
- <sup>27</sup> Department of Physics, Royal Institute of Technology (KTH), AlbaNova, SE-106 91 Stockholm, Sweden
- <sup>28</sup> Science Institute, University of Iceland, IS-107 Reykjavik, Iceland
- <sup>29</sup> email: kamae@slac.stanford.edu
- <sup>30</sup> College of Science, Ibaraki University, 2-1-1, Bunkyo, Mito 310-8512, Japan
- <sup>31</sup> Research Institute for Science and Engineering, Waseda University, 3-4-1, Okubo, Shinjuku, Tokyo 169-8555, Japan
- <sup>32</sup> Department of Astronomy, Stockholm University, SE-106 91 Stockholm, Sweden
- <sup>33</sup> Yukawa Institute for Theoretical Physics, Kyoto University, Kitaashirakawa Oiwake-cho, Sakyo-ku, Kyoto 606-8502, Japan
- <sup>34</sup> Department of Physics, Graduate School of Science, University of Tokyo, 7-3-1 Hongo, Bunkyo-ku, Tokyo 113-0033, Japan
- <sup>35</sup> Center for Research and Exploration in Space Science and Technology (CRESST) and NASA Goddard Space Flight Center, Greenbelt, MD 20771, USA
- <sup>36</sup> Department of Physics and Department of Astronomy, University of Maryland, College Park, MD 20742, USA
- <sup>37</sup> Istituto Nazionale di Fisica Nucleare, Sezione di Roma "Tor Vergata", I-00133 Roma, Italy
- <sup>38</sup> Department of Physics, Boise State University, Boise, ID 83725, USA
- <sup>39</sup> Institute of Space and Astronautical Science, JAXA, 3-1-1 Yoshinodai, Chuo-ku, Sagami-hara, Kanagawa 252-5210, Japan
- <sup>40</sup> Hiroshima Astrophysical Science Center, Hiroshima University, Higashi-Hiroshima, Hiroshima 739-8526, Japan
- <sup>41</sup> email: oxon@mac.com
- <sup>42</sup> Department of Physics and Astronomy, University of Denver, Denver, CO 80208, USA
- <sup>43</sup> Max-Planck-Institut für Physik, D-80805 München, Germany
- <sup>44</sup> Santa Cruz Institute for Particle Physics, Department of Physics and Department of Astronomy and Astrophysics, University of California at Santa Cruz, Santa Cruz, CA 95064, USA
- <sup>45</sup> Institut für Astro- und Teilchenphysik and Institut für Theoretische Physik, Leopold-Franzens-Universität Innsbruck, A-6020 Innsbruck, Austria
- <sup>46</sup> Department of Physics, University of Washington, Seattle, WA 98195-1560, USA

## ABSTRACT

We report on the gamma-ray observations of giant molecular clouds Orion A and B with the Large Area Telescope (LAT) on-board the *Fermi Gamma-ray Space Telescope*. The gamma-ray emission in the energy band between  $\sim 100$  MeV and  $\sim 100$  GeV is predicted to trace the gas mass distribution in the clouds through nuclear interactions between the Galactic cosmic rays (CRs) and interstellar gas. The gamma-ray production cross-section for the nuclear interaction is known to  $\sim 10\%$  precision which makes the LAT a powerful tool to measure the gas mass column density distribution of molecular clouds for a known CR intensity. We present here such distributions for Orion A and B, and correlate them with those of the velocity integrated CO intensity ( $W_{\text{CO}}$ ) at a  $1^\circ \times 1^\circ$  pixel level. The correlation is found to be linear over a  $W_{\text{CO}}$  range of  $\sim 10$  fold when divided in 3 regions, suggesting penetration of nuclear CRs to most of the cloud volumes. The  $W_{\text{CO}}$ -to-mass conversion factor,  $X_{\text{CO}}$ , is found to be  $\sim 2.3 \times 10^{20} \text{ cm}^{-2} (\text{K km s}^{-1})^{-1}$  for the high-longitude part of Orion A ( $l > 212^\circ$ ),  $\sim 1.7$  times higher than  $\sim 1.3 \times 10^{20}$  found for the rest of Orion A and B. We interpret the apparent high  $X_{\text{CO}}$  in the high-longitude region of Orion A in the light of recent works proposing a non-linear relation between  $\text{H}_2$  and CO densities in the diffuse molecular gas.  $W_{\text{CO}}$  decreases faster than the  $\text{H}_2$  column density in the region making the gas “darker” to  $W_{\text{CO}}$ .

*Subject headings:* molecular clouds: general — molecular clouds: individual(Orion A, Orion B)

## 1. Introduction

The Orion A and B clouds are the archetypes of local giant molecular clouds (GMCs) where interstellar gas condenses and stars are formed (e.g., Bergin & Tafalla 2007; Bally 2008, and references therein). The clouds have been studied in various wavebands including millimeter observations of the transition lines between CO rotational states, especially from  $J = 1$  to  $J = 0$  (e.g.,

---

<sup>57</sup>NYCB Real-Time Computing Inc., Lattingtown, NY 11560-1025, USA

<sup>58</sup>Max-Planck Institut für extraterrestrische Physik, 85748 Garching, Germany

<sup>59</sup>Institut für Theoretische Physik and Astrophysik, Universität Würzburg, D-97074 Würzburg, Germany

<sup>60</sup>Institució Catalana de Recerca i Estudis Avançats (ICREA), Barcelona, Spain

<sup>61</sup>Consorzio Interuniversitario per la Fisica Spaziale (CIFS), I-10133 Torino, Italy

<sup>62</sup>INTEGRAL Science Data Centre, CH-1290 Versoix, Switzerland

<sup>63</sup>NASA Postdoctoral Program Fellow, USA

<sup>64</sup>Dipartimento di Fisica, Università di Roma “Tor Vergata”, I-00133 Roma, Italy

Sanders et al. 1984; Maddalena et al. 1986; Dame et al. 1987, 2001; Wilson et al. 2005; Fukui et al. 2011), infrared emission (e.g., Beichman et al. 1988), attenuation of star light (e.g., Dobashi et al. 2005), and near infrared extinction (Rowles & Froebrich 2009; Froebrich & Rowles 2010; Dobashi 2011). The two clouds are prime targets for the Large Area Telescope (LAT) on-board the *Fermi Gamma-ray Space Telescope (Fermi)* in the research of molecular clouds and CR interaction because they lie isolated from the Galactic plane and no intense gamma-ray point source overlaps with the clouds (Abdo et al. 2009d; Abdo et al. 2010b).

Gamma rays from the Orion-Monoceros region were first detected by COS-B in the energy range between 100 MeV and 5 GeV (Caraveo et al. 1980; Bloemen et al. 1984). EGRET detected gamma rays in the range between 100 MeV and  $\sim 10$  GeV (Digel et al. 1995, 1999). In these studies, the gamma-ray intensity distribution in a region including Orion A, B and Monoceros R2 was fitted with three independent contributions, one proportional to the atomic hydrogen (H I) column density, another proportional to the CO line intensity ( $W_{\text{CO}}$ )<sup>1</sup>, and the last, a presumed isotropic distribution. Under the assumptions that  $W_{\text{CO}}$  traces the H<sub>2</sub> column density, the CR spectrum doesn't change in the region and H I spin temperature ( $T_S$ ) is constant, the ratio  $X_{\text{CO}}$  was determined<sup>2</sup>, from the ratio of the gamma-ray intensities associated with the H I and CO distributions, to be  $X_{\text{CO}} = (2.6 \pm 1.2) \times 10^{20} \text{ cm}^{-2} (\text{K km s}^{-1})^{-1}$  (Bloemen et al. 1984) and  $X_{\text{CO}} = (1.35 \pm 0.15) \times 10^{20} \text{ cm}^{-2} (\text{K km s}^{-1})^{-1}$  (Digel et al. 1999). The ratio was not separately measured for the three clouds, Orion A, B and Monoceros R2, due to the limited statistics and spatial resolution of the instruments. We note that Strong et al. (1988) determined  $X_{\text{CO}}$  on the diffuse Galactic gamma rays observed by COS-B to be  $X_{\text{CO}} = (2.3 \pm 0.3) \times 10^{20} \text{ cm}^{-2} (\text{K km s}^{-1})^{-1}$  and Dame et al. (2001), by comparing smoothed infrared intensity and  $W_{\text{CO}}$  distributions across the Galaxy, determined it to be  $X_{\text{CO}} = (1.8 \pm 0.3) \times 10^{20} \text{ cm}^{-2} (\text{K km s}^{-1})^{-1}$ .

Since the publications on the EGRET data (Digel et al. 1995, 1999), much progress has been made in studies on Orion A and B: new observational data became available (e.g., Dame et al. 2001; Lombardi & Alves 2001; Wilson et al. 2005; Kalberla et al. 2005; Dobashi et al. 2005; Rowles & Froebrich 2009; Froebrich & Rowles 2010; Dobashi 2011); study of the molecular clouds was renewed (e.g., Wilson et al. 2005; Bally 2008); a new modeling of the Galactic diffuse gamma-ray emission was proposed incorporating large-scale CR propagation (Strong & Moskalenko 1998; Strong et al. 2000); theoretical calculations of collisional CO rotational-level excitation were revisited (Mengel et al.

---

<sup>1</sup>We define  $W_{\text{CO}}$  as the velocity-integrated intensity of the transition line between  $J = 1$  to  $J = 0$  in  $^{12}\text{C}^{16}\text{O}$ .

<sup>2</sup>Our  $X_{\text{CO}}$  is a factor converting  $W_{\text{CO}}$  to mass column density measured in units of the proton mass in cloud concentrations predominantly consisting of H<sub>2</sub>. In some literature  $X_{\text{CO}}$  is used as the factor converting  $W_{\text{CO}}$  to H<sub>2</sub> column density. Where  $W_{\text{CO}}$  traces H<sub>2</sub> accurately and the chemical state of hydrogen is predominantly in H<sub>2</sub>, the 2 definitions are expected to agree. The helium and heavier atoms are assumed to be mixed uniformly in the interstellar gas with the solar abundance. We warn readers that comparison of  $X_{\text{CO}}$  values calculated on different CO surveys and gamma-ray observations are not straightforward due to differences in their calibration procedure (e.g. see Bronfman et al. 1988, for the CO calibration factor) as well as in the assumptions on the CR composition and the associated cross-sections.



2001; Flower 2001; Cecchi-Pestellini et al. 2002; Balakrishnan et al. 2002; Wernli et al. 2006; Shepler et al. 2007; see also Kalberla et al. 2005; Liszt 2006, 2007) and the distance to the Orion nebula in the Orion A cloud was measured accurately (Sandstrom et al. 2007; Menten et al. 2007; Hirota et al. 2007; Kim et al. 2008).

The *Fermi* Gamma-ray Space Telescope mission, launched on 2008 June 11, has been surveying the sky with the Large Area Telescope (LAT) since 2008 August. Its wide field of view, large effective area, improved spatial resolution, and broad energy coverage provide much higher sensitivity relative to its predecessor EGRET (Atwood et al. 2009; Abdo et al. 2009a).

Studies based on EGRET observations have established that gamma rays from Galactic molecular clouds are dominated by neutral pion decays (which we refer to as the “pionic gamma rays” or “pionic emission”) in the energy band between 0.2 GeV and 10 GeV (Bertsch et al. 1993; Digel et al. 1995, 1999). Orion A and B are located far ( $\sim 8.8$  kpc) from the Galactic center<sup>3</sup> and displaced from the Galactic plane by  $\sim 140$  pc. The two clouds are only  $\sim 400$  pc away from the solar system where spectra of CR species upto the sub-TeV domain are predicted to be similar to those measured directly at the Earth after correction for the solar modulation.

We can now analyze Orion A and B through the high-energy gamma rays detected by the *Fermi* LAT in the light of the recent developments and study the relation between  $W_{\text{CO}}$  and mass column density (or  $X_{\text{CO}}$ ) in various parts of the Galaxy and obtain the total mass of the clouds<sup>4</sup>. The improved spatial resolution and higher gamma-ray statistics provided by the *Fermi*-LAT allow us to determine the relation on angular scales of  $1 \times 1 \text{ deg}^2$  (pixels), without being directly affected by the thermodynamical, chemical, or radiation environment inside the Orion clouds, albeit within the limited angular resolution of the *Fermi* LAT and uncertainties due to any unresolved weak sources and CR flux variation. The results can be used conversely to study various environmental effects on  $X_{\text{CO}}$  in the translucent parts of clouds where most gas in Orion A and B resides and where the  $X_{\text{CO}}$  factor has not been straightforward to derive (e.g., van Dishoeck & Black 1986; Magnani et al. 1988; Bolatto et al. 1999; Magnani et al. 2003; Bell et al. 2006; Snow & McCall 2006; Bell et al. 2007; Burgh et al. 2007; Wall 2007; Sheffer et al. 2008).

Theoretical analyses have long suggested that  $X_{\text{CO}}$  depends on the environment and the  $W_{\text{CO}}-N(\text{H}_2)$  relation may be nonlinear (e.g., Kutner & Leung 1985; Dickman et al. 1986; Maloney & Black 1988; Taylor et al. 1993; Bolatto et al. 1999; Magnani et al. 2003; Bell et al. 2007; Burgh et al. 2007). Suggestions have also been made that  $X_{\text{CO}}$  depends on the relative abundances of CO, C I, and C II (e.g. van Dishoeck & Black 1988; Hollenbach et al. 1991; Kopp et al. 2000). The existence of gas not traced by H I and CO at the interface between the two phases (the “dark gas”) has been

---

<sup>3</sup>We assume the distance between the Sun and the Galactic center to be 8.5 kpc and the Galactic rotation velocity near the Sun to be  $220 \text{ km s}^{-1}$ .

<sup>4</sup>The mass of Orion A and B is distributed mostly in the column density range corresponding to a “translucent” cloud whose line-of-sight visual attenuation ( $A_V$ ) is typically between 1 and 5 mag and has  $n(\text{H}_2)$  typically between 100 and  $2000 \text{ cm}^{-3}$  (e.g. van Dishoeck & Black 1988).

discovered (Grenier et al. 2005; Ade et al. 2011). The relation between the fraction of carbon in CO and H<sub>2</sub> density in translucent and diffuse clouds has been updated based on observations and numerical simulations, for example, by Burgh et al. (2010); Wolfire et al. (2010); Glover et al. (2010). Our results will be interpreted in the light of these recent works. The  $W_{\text{CO}}-N(\text{H}_2)$  relation will be characterized including the “dark gas,” and the measured mass column density will be related to the  $A_V$  value at which the relation is predicted to become non-linear.

In this paper we analyze diffuse gamma rays spatially associated with the molecular clouds<sup>5</sup> Orion A and B, extract their pionic gamma-ray components, obtain mass distributions, and compare them with those predicted for  $W_{\text{CO}}$  measured by Fukui et al. (2011) and Dame et al. (2001). In Section 2 we describe the gamma-ray event selection applied in this analysis. The analysis procedure is described in Section 3 in 4 subsections: the spatial templates used to extract mass column density associated with multiple emission components are given in Subsection 3.1; energy-binned spatial fits on the templates are described in Subsection 3.2; the pionic emission is extracted from the spectra obtained in the spatial fits and  $X_{\text{CO}}$  is calculated thereon in Subsection 3.3; and the total H<sub>2</sub> masses of Orion A and B are estimated in Subsection 3.4. In Section 4, we assess systematic uncertainties in the analyses; check the  $X_{\text{CO}}$  results with recent infrared excess emission maps by Dobashi (2011); summarize the results; and interpret them in the light of recent studies of the relation between the H<sub>2</sub> and CO fraction in the translucent clouds. The paper is concluded in Section 5.

## 2. Observations and Data

The data used in this analysis were obtained in the nominal all-sky survey mode between 2008 August 4 and 2010 March 11<sup>6</sup>. We select events classified as *Pass6 Diffuse* class which has a high gamma-ray purity (Atwood et al. 2009). Among the events, we limit the reconstructed zenith angle to be less than 105° to greatly reduce gamma rays coming from the limb of the Earth’s atmosphere. We select the good time intervals (GTIs) of the observations by excluding events that were taken while the instrument rocking angle was larger than 52°. Another cut is made on the reconstructed gamma-ray energy at  $E_{\text{min}} = 178$  MeV and  $E_{\text{max}} = 100$  GeV to reduce systematic uncertainty of the LAT effective area and residual background events induced by CRs. Gamma rays in a rectangular region of 30° × 30° centered at ( $\ell = 210^\circ$ ,  $b = -20^\circ$ ) are then selected for later analyses. We refer to the region as the region-of-interest (ROI) and the set of events as the data set.

---

<sup>5</sup>By molecular clouds we mean spatially identified clouds without distinguishing the small admixture of atomic and ionized hydrogens therein.

<sup>6</sup>Mission Elapsed Time 239,557,413 s through 290,000,000 s where zero is set at 00:00 UTC on 2001 January 1. During the period, the LAT was operated in the survey mode with the rocking angle 35 deg (2008 August 4 to 2009 July 9), 39 deg (2009 July 9 to 2009 September 3) and 50 deg (2009 September 3 to 2010 March 11).

The data set consists of 1,132,436 events of which 901,929 are between 178 MeV and 1 GeV, 224,753 between 1 GeV and 10 GeV, and 5,754 between 10 GeV and 100 GeV. They are binned in  $150 \times 150$  equal-area pixels (Hammer-Aitoff projection) in Galactic coordinates with  $0.2^\circ$  gridding on their reconstructed arrival directions, and in 22 logarithmic bins between  $E_{\min} = 178$  MeV and  $E_{\max} = 100$  GeV on their reconstructed energies.

The map of counts integrated over the energy range of the data set is shown in Fig. 1. We can visually identify Orion A and B near the center of the region and the outer Galactic plane in the upper part. We note that Monoceros R2 is also visible between Orion A/B and the outer Galactic plane.

### 3. Analyses

The analyses presented here begin by finding the relationship between the spatial distributions of gamma rays and  $W_{\text{CO}}$ , the most widely used proxy of  $\text{H}_2$ , in the Orion clouds and by studying the proportionality between the two and its spatial dependence within the Orion clouds. The analyses proceed in 3 steps.

In the first step, the spatial distribution of the “background” gamma rays, i.e., the gamma rays not associated with the  $\text{H}_2$  clouds, is determined by using spatial distribution templates, for the H I gas, for the inverse Compton scattering (IC) component, for the point sources, and for a presumed isotropic component (Subsections 3.1). We then fit, in Subsection 3.2, the gamma-ray spatial distribution in each of the 22 energy bins as a sum of the “background” distribution and a distribution tentatively associated with the  $\text{H}_2$  gas ( $\text{H}_2$ -template). The “background” is subtracted from the measured gamma-ray intensity distribution and the remainder is defined as the gamma-ray intensity distribution associated with the  $\text{H}_2$  gas with which  $W_{\text{CO}}$  is correlated pixel-by-pixel. We note that the gamma-ray intensity measures the mass column density in the  $\text{H}_2$  gas for a known CR spectrum. We repeat the fit with 2 alternative  $\text{H}_2$ -templates.

In the second step (Subsections 3.3 and 3.4), the energy-binned gamma-ray emissivity for the  $\text{H}_2$  gas ( $B_i$  in eq. (1)) are assembled as the gamma-ray spectrum for each of the 3  $\text{H}_2$ -templates. The spectrum is then fitted as a sum of the gamma rays produced in the pionic and bremsstrahlung processes.

In the third step, the gamma-ray intensity distribution associated with the pionic emission is converted to the mass column density. The  $W_{\text{CO}}$ -mass conversion factor ( $X_{\text{CO}}$ ) is calculated via two methods, one by comparing the gamma-ray counts associated with the H I gas and with the  $\text{H}_2$  gas (the  $\text{H}_2/\text{H I}$  method) and the other by dividing the gamma-ray counts of the pionic emission by the number of pionic gamma rays expected per unit gas mass (the pionic method). In the first method, we assume the CR spectrum is uniform in the local H I region within Galactocentric radius of 8 – 10 kpc (see Subsection 3.1.1) and in the Orion clouds. In the latter method, we assume the CR spectrum including its absolute flux is known in the Orion clouds. We validate



these assumption using GALPROP.

We use GALPROP (Strong & Moskalenko 1998; Strong et al. 2000) with the parameter set labeled as GALDEF 54.77Xvarh7S. This parameter set is known to reproduce reasonably well the Galactic diffuse gamma-ray emission observed with the LAT (Abdo et al. 2009f)<sup>7</sup>. We refer to the results obtained by running GALPROP with this parameter set as the GALPROP results in this paper.

### 3.1. Spatial distribution templates

Initially we assume the gamma-ray emission from the ROI to be made of 4 “background” components and one “signal” H<sub>2</sub> component, each emitting gamma rays with a characteristic spatial distribution. The 4 “background” components are spatially associated with the diffuse H I gas, the inverse Compton (IC) scattering by electrons<sup>8</sup> off interstellar radiation fields, the point sources, and the sum of extragalactic diffuse emission (including unresolved sources) and backgrounds induced by CRs in the instrument. We assume the last sum to be isotropic and refer to it as the isotropic component. We ignore the contribution from ionized hydrogen gas (H II) because its density is low when averaged in  $1 \times 1 \text{ deg}^2$  pixels ( $< 0.5 \text{ cm}^{-3}$ ) and its total mass is negligible in the ROI (Gordon 1969; O’Dell 2001).

All spatial components except for the IC component are assumed to have, individually, an energy-independent underlying spatial distribution in Galactic coordinates  $(l, b)$ . Another important underlying assumption is that the nuclear CR spectrum is uniform over the ROI. We make spatial templates for the 22 energy bins by convolving the spatial distributions with the energy-dependent point spread function (PSF) and exposure for the individual energy bins. Hence the spatial templates are energy dependent. In Subsection 3.3 we will show that the spectra of the gamma-ray emissions associated with the H I and H<sub>2</sub> gas consist of the pionic and bremsstrahlung components.

The gamma-ray intensity  $I_\gamma(l, b)$  for the  $i$ -th energy bin is interpreted as the sum of the five contributions, each being the product of the normalization factor for the  $i$ -th energy bin and the spatial template.

$$I_{\gamma,i}(l, b) = A_i N(\text{H I})(l, b) + B_i N(\text{H}_2)(l, b) + IC_i(l, b) + \sum_j (C_{ij} \delta_{l_j, b_j}) + D_i, \quad (1)$$

The normalization factors are:  $A_i$  for the H I gas;  $B_i$  for the component associated with clouds consisting predominantly of H<sub>2</sub>;  $IC_i$  for the inverse Compton component;  $C_{ij} \delta_{l_j, b_j}$  for the  $j$ -th point

<sup>7</sup>A detailed description of GALDEF files can be found at <http://galprop.stanford.edu>.

<sup>8</sup>We refer to electrons as a sum of  $e^+$  and  $e^-$ .

source at  $(l_j, b_j)$ ; and  $D_i$  for the isotropic component which is assumed not to depend on  $(l, b)$ . The normalization factors are determined independently for the 22 energy bins. We note that  $IC_i$  are fixed at the values given by GALPROP, because the spatial distribution is highly correlated with the isotropic component, and the IC component is sub-dominant in the ROI.

Later in Subsection 3.2, we will explore 3 templates for  $H_2$ , two based on  $W_{CO}$  and one on  $W_{CO}$  plus the “dark gas” proposed by Grenier et al. (2005).

### 3.1.1. Diffuse H I gas template

Atomic hydrogen gas (H I) is broadly distributed in the Galaxy with a total mass exceeding that of molecular hydrogen ( $H_2$ ) (e.g., Ferrière 2001; Snow & McCall 2006). In the outer Galaxy where the Orion clouds are located, the mass column density of H I is lower than that of  $H_2$  at the Orion clouds (Kalberla et al. 2010, 2005)

We used the Leiden/Argentine/Bonn (LAB) survey data (Kalberla et al. 2005) corrected for optical thickness by adopting a constant spin temperature ( $T_S$ ) of 125 K as the H I gas spatial distribution template (see Fig. 2a). The LAB intensity distribution is divided into five annuli centered at the Galactic center as has been done in other *Fermi* diffuse emission analyses (Abdo et al. 2010c). Their inner and outer Galactocentric radii ( $R$ ) are: 8 to 10, 10 to 11.5, 11.5 to 16.5, 16.5 to 19, and 19 to 50 kpc. The line-of-sight velocity distribution of the H I gas in the Orion region overlaps that of the CO gas associated with the Orion clouds and that of the local H I annulus ( $R = 8 - 10$  kpc) quite well.

Gamma-ray contributions from all the H I annuli overlapping our ROI have been included in the analyses. In the fitting, the CR intensity is treated independently at each annulus. The contributions from annuli other than the local one ( $R = 8 - 10$  kpc) are through the periphery of the LAT PSF and less than  $\sim 5\%$  in gamma-ray counts. Hence our analyses are insensitive to variation in the CR intensity and/or spectrum among the neighboring annuli.

The spin temperature of H I gas,  $T_S$ , is not well constrained in the region nor known to be uniform over the ROI: its quoted value in the literature ranges between  $\sim 90$  K and  $\sim 400$  K (e.g. Mohan et al. 2004a,b). We estimate, later in this paper, the contribution to the overall systematic error from this uncertainty by repeating the analysis for  $T_S = 250$  K and 90 K. No significant concentration of cold H I is known around Orion A and B at large-scale ( $> 1 \times 1 \text{ deg}^2$ ) (Kalberla et al. 2010). An exploratory study of cold H I mixed in selected  $H_2$  cloud cores has found the mean H I fraction to be less than 0.5% (Krčo et al. 2008). So we can safely ignore such a mixture in the analysis.

Gamma rays are produced in the H I gas through the pionic and bremsstrahlung processes with intensities proportional to the CR nuclear and electron spectra in the gas, respectively.

### 3.1.2. Molecular cloud template

We try 3  $H_2$  templates to represent the  $H_2$  spatial distribution in the ROI. In making the templates we assume that the  $H_2$  column density is proportional to  $W_{CO}$  measured by two CO ( $J = 1 \rightarrow 0$ ) surveys, one from NANTEN (Fukui et al. 2011) covering the areas around the Orion clouds with effective resolution of  $4'$  and the other being the Galactic survey by Dame et al. (2001) covering the ROI with angular resolution of  $8.7'$ . The spatial distributions indicated by the two surveys are mutually consistent at the angular scale of the LAT PSF except for the overall normalization.

The first  $H_2$  template,  $H_2$ -template-1, is made by combining the two surveys and accounting for their relative intensity scales (Fig. 2b): NANTEN  $W_{CO}$  for the area defined by the solid white line and that by Dame et al. (2001) for the rest of the region. We refer to the 3 regions defined by dashed lines in Fig. 3b as “the 3 Orion regions” hereafter<sup>9</sup>. We scale the NANTEN data by the factor  $1/1.11$  to adjust the intensities to a common scale with Dame et al. (2001) because the survey by Dame et al. (2001) has been widely used in gamma-ray analyses.

We first start the analyses by setting one common  $B_i$  factor for  $W_{CO}$  in the ROI ( $H_2$ -template-1), or equivalently, one common  $X_{CO}$  for the entire ROI. In the second  $H_2$  template,  $H_2$ -template-2, the  $W_{CO}$  distribution is divided into 4 regions (the 3 Orion regions and the rest of the ROI) and allow  $B_i$ , or equivalently  $X_{CO}$ , to be different in each region. We add a “dark gas” template (Grenier et al. 2005) to  $H_2$ -template-1 to make the third  $H_2$  template,  $H_2$ -template-3 (Fig. 2a and 2c). The normalization is set free for the 2 templates.

These spatial templates are described further in the subsections to follow.

### 3.1.3. Inverse Compton template

The inverse Compton component is known to be minor around the Orion clouds. We use the IC spectrum and spatial distribution given by GALPROP where the interstellar photon fields are taken from Porter et al. (2008). The typical Galactic-scale IC intensity in the region is  $\sim 5$  times smaller than the isotropic component described later, and their spatial and spectral distributions are similar in this region. Possible local enhancement is the IC emission around the Orion Nebula (M42) where strong ultraviolet emission (e.g. Murthy et al. 2005) and moderate infrared emission (e.g. Prisinzano et al. 2008) exists. According to our calculation, such IC emissions are not detectable with the current LAT sensitivity (Orlando & Strong 2008).

---

<sup>9</sup>The boundaries are: Orion A Region I ( $217^\circ > \ell > 212^\circ$ ,  $-23^\circ < b < -16^\circ$ ), Orion A Region II ( $212^\circ > \ell > 205^\circ$ ,  $-23^\circ < b < -16^\circ$ , excluding the overlap with Orion B), and Orion B ( $209^\circ > \ell > 203^\circ$ ,  $-18^\circ < b < -13^\circ$ )

### 3.1.4. Point sources in the Orion region

More than 1400 point sources are reported in the First *Fermi* LAT Catalog (Abdo et al. 2010b). Among them, 30 point sources are in our ROI,  $(l, b) = (210 \pm 15^\circ; -20 \pm 15^\circ)$ . There are an additional 29 sources within 5 deg of the ROI. In the likelihood fit to be discussed later, the normalization is set free, energy-bin by energy-bin, for 25 high-confidence sources in the ROI; the indexes and normalizations are fixed to the values given in the First *Fermi* LAT Catalog (Abdo et al. 2010b) for those outside of the region. There are 5 low-confidence sources (or candidates) overlapping with the clouds: they are<sup>10</sup> 1FGL J0540.4–0737c, J0536.2–0607c, J0534.7–0531c, J0541.9–0204c, and J0547.0+0020c. Their fluxes are all low and labeled as “c” in the catalog, meaning either their flux estimates are uncertain, or they can be artifacts resulting from incorrect modeling of the Galactic diffuse emission. We fit the spatial templates and analyze the spectra in the 3 Orion regions with and without them. The results we quote will be for the analyses without them: we include their possible contribution in the systematic error.

### 3.1.5. Isotropic component

In the present analyses, the extragalactic emission and residual CR background in the data are not separated but treated as a single isotropic component (Abdo et al. 2009c, 2010c; Ackermann et al. 2010; Abdo et al. 2010a). The total flux of the component at 1 GeV is  $\sim 25\%$  of that associated with  $H_2$  when averaged over the 3 Orion regions (subtending  $\sim 30$  msr) defined around Orion A and B (see Fig. 3b).

The residual background in the *Pass6 Diffuse* class consists of CR-induced events misclassified as gamma rays and CRs that converted in the passive material just outside of the LAT without leaving a signal in the anti-coincidence detector (Atwood et al. 2009). When averaged over many orbits of observations, the residual background can be approximated as isotropic.

## 3.2. Fit to the Spatial Distribution

All spatial templates described in the previous subsection were convolved with the LAT exposure and PSF. The spatial fit is made using the binned likelihood program *gllike* included in the *Fermi* ScienceTools<sup>11</sup> and the  $\ddagger$  normalizations ( $A_i$ ,  $B_i$ ,  $C_{ij}$  and  $D_j$ ) in Eq. (1) are determined independently for the 22 energy bins. We note again that  $IC_i$  are fixed at the values given by GALPROP. Each H I annulus has a separate  $A_i$ . We report only  $A_i$  for the local annulus as others are not determined well because they lie mostly outside of our ROI.

---

<sup>10</sup>No new sources have been added in this region in the Second *Fermi* LAT Catalog (Abdo et al. 2011).

<sup>11</sup>We use ScienceTools version v9r16p0 with *P6.V3.DIFFUSE* instrument response functions.

Our scientific interest is to study the contributions from the gas concentrations identified as Orion A and B, which are believed to be predominantly  $\text{H}_2$ . We consider, hence, the sum of the H I, IC, point-source, and isotropic components as the “background” which is determined by fitting the observed gamma-ray distribution for each of the 22 energy bins. In the fits, we assume that  $\text{H}_2$ -template-1, or the  $W_{\text{CO}}$  distribution, represents approximately the  $\text{H}_2$  distribution. The gamma-ray distribution associated with the  $\text{H}_2$  gas can be extracted less dependently on yet-unknown  $\text{H}_2$ - $W_{\text{CO}}$  relation by subtracting the “background” from the observed gamma-ray distribution.

We define 2 improved  $\text{H}_2$ -templates,  $\text{H}_2$ -template-2 and 3 after the initial analysis on  $\text{H}_2$ -template-1. The spatial distribution is not proportional to  $W_{\text{CO}}$  for the 2 improved templates and hence the “background” is different for each  $\text{H}_2$ -template by a small amount. The difference is however negligible.

### 3.2.1. Spatial Fit with $W_{\text{CO}}$ of One $X_{\text{CO}}$ : $\text{H}_2$ -template-1

We use  $\text{H}_2$ -template-1 as an approximation for the  $\text{H}_2$  gas distribution and fit Eq. (1) to determine the “background”. The energy-summed gamma-ray distribution after subtracting the “background” is shown in Fig. 3a and that of the  $W_{\text{CO}}$ -based model, or the product of  $\Sigma B_i$  in Eq. (1) and  $\text{H}_2$ -template-1, is given in Fig. 3b. The two count distributions are correlated pixel-by-pixel ( $1 \times 1 \text{ deg}^2$ ) in the 3 Orion regions in Fig. 4a. We expect a good linear correlation between the two if  $W_{\text{CO}}$  is a good tracer of  $\text{H}_2$ .

We note first that the correlation is fairly linear and gives a correlation coefficient<sup>12</sup> of 0.93. We then note that the correlation significantly improves if we separate the Orion clouds into the 3 Orion regions, Orion A Region I (black solid line) and II (red dashed line), and Orion B (blue dotted line). The correlation coefficients for the 3 Orion regions are 0.98, 0.96, and 0.98, and the best-fit slopes are 0.72, 0.99, and 1.25, respectively.

The large difference ( $\sim 40 - 60\%$ ) in the best-fit slope suggests that the mass column density in Orion A and B cannot be simply derived using the same value of  $X_{\text{CO}}$ . We find more gamma rays in Orion A Region I per  $W_{\text{CO}}$  than in Orion A Region II and Orion B, suggesting  $X_{\text{CO}}$  is different in the 3 Orion regions, or that some fraction of the  $\text{H}_2$  gas is not traced by  $W_{\text{CO}}$  provided a uniform CR density. We explore these two possibilities by redefining the  $\text{H}_2$ -template.

### 3.2.2. Spatial Fit with $W_{\text{CO}}$ of 4 different $X_{\text{CO}}$ values: $\text{H}_2$ -template-2

Based on the relation found between the spatial distributions of the gamma-ray intensity associated with the  $\text{H}_2$  gas and the  $W_{\text{CO}}$ -based model ( $\text{H}_2$ -template-1), we make a second template,

---

<sup>12</sup>The correlation coefficient is defined as  $\Sigma(x - \bar{x})(y - \bar{y}) / \sqrt{\Sigma(x - \bar{x})^2 \Sigma(y - \bar{y})^2}$



H<sub>2</sub>-template-2, that will delineate the H<sub>2</sub> column density more faithfully. In the template we divide the ROI into 4 regions, the 3 Orion regions and the rest of the ROI, and allow  $B_i$  to be different in each region, or introduce 4  $B_i$ 's.

The fitted results for  $A_i$  (H I) and  $B_i$  (H<sub>2</sub>-template-2) in Eq. (1) are listed in Table 1 after combining the highest 10 energy bins into 3 bins. The gamma-ray count map is shown in Fig. 3c is the sum of the 4  $B_i$ 's multiplied with the corresponding components of H<sub>2</sub>-template-2. We note that the 3 Orion regions mix to some degree through the *Fermi* PSF. The correlation between the gamma-ray distribution associated with H<sub>2</sub> and the H<sub>2</sub> template improved as shown in Fig. 4b: the best-fit slopes for Orion A Region I, Region II and Orion B are 0.95, 0.94, and 1.03, respectively, while the correlation factors remain almost the same, 0.98, 0.99, and 0.96, respectively.

The  $X_{\text{CO}}$  for the 4 regions can be calculated directly as the ratio of  $B_i$  to  $2A_i$  (the H<sub>2</sub>/H I method) or by extracting the gamma-ray emission in the regions (the pionic method). The results from the former are given in Table 2 together with those from the latter which will be described in Subsection 3.3.

### 3.2.3. Spatial fit with $W_{\text{CO}}$ and "dark gas": H<sub>2</sub>-template-3

Grenier et al. (2005) found that a significant fraction of local diffuse gamma-ray emission observed by EGRET is not associated with either H I or  $W_{\text{CO}}$ , but rather with the dust map traced by thermal infrared emission given by Schlegel et al. (1998). The missing gas component is often referred to as the "dark gas". Other LAT observations have found gamma rays associated with such "dark gas" (Abdo et al. 2010c; Ackermann et al. 2010). We note recent measurements of attenuation or reddening of background stars have also detected gas concentrations not traced well by  $W_{\text{CO}}$  (Dobashi et al. 2005; Rowles & Froebrich 2009; Dobashi 2011; Ade et al. 2011).

We make a third template, H<sub>2</sub>-template-3, that can bring out the true gas distribution associated with the Orion clouds and enhance our understanding of the  $W_{\text{CO}}$ -to-H<sub>2</sub> relation by introducing the "dark gas". The new H<sub>2</sub> template consists of H<sub>2</sub>-template-1, or  $W_{\text{CO}}$ , and a "dark gas" spatial template with a normalization factor for each.

Our "dark gas" template has been produced following the prescription given by Grenier et al. (2005) and referred to as  $E(B - V)_{\text{res}}$ . It is a residual map obtained by subtracting the best-fit linear combination of  $N(\text{H I})$  and  $W_{\text{CO}}$  from the  $E(B - V)$  map of Schlegel et al. (1998) as described in Ackermann et al. (2010). Fig. 2c shows the  $E(B - V)_{\text{res}}$  map around our ROI. There is a problem with the color temperature correction of the map by Schlegel et al. (1998) around the OB associations in the Orion A and B clouds, and thus  $E(B - V)_{\text{res}}$  value is negative in these points. We masked out these pixels in the  $E(B - V)_{\text{res}}$  map by setting the corresponding values to zero.

The results for  $A_i$  (H I) and  $B_i$  (2 normalizations, one for  $W_{\text{CO}}$  and one for the "dark gas") in

Eq. (1) are listed after combining the highest 10 energy bins into 3 bins in Table 3. The distribution of the gamma-ray counts associated with  $H_2$ -template-3, the sum of the counts associated with  $W_{CO}$  and the “dark gas”, is given in Fig. 3d. The correlation between the extracted gamma-ray counts and the model counts improves as shown in Fig. 4c, bringing the correlation coefficients to 0.99, 0.99, 0.97, and 0.98, for Orion A Region I, Region II, Orion B and the sum of the 3 regions, respectively. The improvement in the correlation, or equivalently in the spatial fit, comes from inclusion of  $E(B - V)_{res}$  which has the largest contribution in the Orion A Region I seen in Fig. 2c.

#### 3.2.4. Summary of the Spatial Fits

The relative likelihoods of the spatial fits with Eq. (1) in the ROI are compared among the 3  $H_2$ -templates in Fig. 5 for the 22 energy bins. The “dark gas” template ( $H_2$ -template-3) gives the best fit in almost all energy bins and the 3- $X_{CO}$  template ( $H_2$ -template-2) gives the second best result. The improvements relative to  $H_2$ -template-1 are statistically significant.

The residuals of the fits with the 3 templates in the ROI are given in Fig. 6. The rectangular boundaries of the 3 Orion regions shown in Figs. 3b, c, d are replicated in the figure. The residuals are significant within the Orion regions for  $H_2$ -template-1 (Fig. 6a) but not for the other 2 templates (Fig. 6b, c), which is consistent with the improvement we saw in Fig. 4. The difference in the residuals for  $H_2$ -template-2 and  $H_2$ -template-3 in the Orion regions is not significant relative to the systematic uncertainty discussed in the next subsection. We find that the large improvement  $H_2$ -template-3 has brought relative to  $H_2$ -template-2 in Fig. 5 comes primarily from outside of the 3 Orion regions, especially in the Monoceros R2 region and in the northern region adjacent to the Orion B: the template adds “dark gas” in that part whereas the other templates only modify the 3 Orion regions.

The value of  $X_{CO}$  has been calculated by the  $H_2/H\ I$  method by taking the ratio of  $B_4$  to  $2A_4$  for the parts associated with  $W_{CO}$  in the  $H_2$ -templates and listed in Table 2. In the pionic method of evaluating  $X_{CO}$ , however, the pionic component must be extracted out of the gamma-ray spectrum associated with the  $H_2$ -template as will be described in Subsection 3.3. We will discuss the systematic errors in evaluating  $X_{CO}$  and possible interpretations of the results in Section 4.

### 3.3. Analyses of Spectra

The spectra associated with the  $H\ I$  and  $H_2$ -template-1, with the  $H\ I$  and  $H_2$ -template-2, and with the  $H\ I$  and  $H_2$ -template-3 are obtained by assembling the fitted results for the respective templates,  $A_4$  and  $B_4$ , as shown in Figs. 7, 8, and 9, respectively. The spectra are fitted as a sum of the pionic and bremsstrahlung components. The gamma-ray spectra associated with the spatial templates ( $H\ I$ , inverse Compton, isotropic, and sum of  $X_{CO} \times W_{CO}$ ) are plotted for the 3 Orion regions in Fig. 10a and b. We analyze for the gamma rays associated with the 3  $H_2$ -templates in

this subsection.

### 3.3.1. Fit with Gamma-ray Emission Models

The spectral template of pionic gamma rays has been calculated by convolving the gamma-ray inclusive cross-section for  $p-p$  interaction parameterized by Kamae et al. (2006) and the CR proton spectrum predicted by GALPROP at the Orion clouds.<sup>13</sup> The proton flux is predicted in the Orion clouds ( $R = 8.8$  kpc,  $Z = -0.14$  kpc) to be  $\sim 8\%$  smaller than that at the solar system ( $R = 8.5$  kpc,  $Z = 0.0$  kpc) where the GALPROP proton spectrum has been determined by the CR data taken at the Earth. The value at the Orion clouds is consistent with that determined using the gamma rays from the local H I (Abdo et al. 2009c). The good fit to the data seen Figs. 7, 8, and 9 supports GALPROP's prediction of CR spectral shape in the Orion region and the overall modeling of Eq. (1).

Bremsstrahlung emission induced by CR electrons interacting with gas is calculated in GALPROP using recent bremsstrahlung calculations (Strong & Moskalenko 1998; Strong et al. 2000, and references therein). The electron injection spectrum in our GALPROP calculation had been adjusted to reproduce, approximately, the power-law index of the electron spectrum measured by the *Fermi* LAT (Abdo et al. 2009e). In addition, the normalization of the spectrum is adjusted to reproduce the LAT observed gamma-ray flux at a low-energy band. In the spectral fits described below, we kept the electron-to-proton ratio, or equivalently the bremsstrahlung-to-pion ratio, fixed to the value given in GALPROP. When we refer to the gamma-ray emissivity per atom or molecule, we do not differentiate the underlying processes, but rather the sum of the bremsstrahlung and pionic contributions.

The spectral fit of the H I component is reasonable for all 3  $H_2$  templates ( $\chi^2 = 17.7, 9.9,$  and  $17.1$  for  $\text{dof} = 14$  respectively) as shown in Figs. 7a, 8a and 9a. Our pionic flux associated with H I is consistent with that obtained in the *Fermi* study on the local interstellar gas (Abdo et al. 2009c) as overlaid in Fig. 8a. We note however that there may be a small offset between the two as will be discussed later. The spectra associated with molecular clouds are also fitted well by the 3  $H_2$ -templates as shown below.

The mass-to- $W_{CO}$  ratio,  $X_{CO}$ , can be obtained by comparing the assumed pionic gamma-ray emissivity per H atom with the observed gamma-ray emissivity per  $W_{CO}$  as shown in Figs. 7b,

---

<sup>13</sup>In GALDEF 54.77Xvarh7S, the CR proton flux was artificially multiplied by 1.15 to reproduce gamma-ray observations by *Fermi*. The factor originates from the underestimate of gamma-ray emissivity for He and heavier atoms in the interstellar medium (ISM) in GALPROP. Instead of using the 1.15 correction factor, we combined the calculation by Gaisser & Schaefer (1992) for contributions from CR He and heavier atoms, and the calculation by Mori (2009) for heavier atoms in the ISM. Hence the total gamma-ray emissivity per H atom is 1.70 times larger than that for  $p-p$  collisions only. The difference between the total gamma-ray emissivity in the two literatures is  $\sim 5\%$ , which is taken into account in the systematic uncertainty.

8b–d and 9b. The former is calculated in the unit of  $\text{MeV}^{-1}\text{s}^{-1}\text{sr}^{-1}$ , and the latter is measured in the unit of  $\text{MeV}^{-1}\text{s}^{-1}\text{sr}^{-1}(2 \times 10^{20}\text{cm}^{-2}(\text{K km s}^{-1})^{-1})^{-1}$ . Thus,  $X_{\text{CO}}/2$  of the clouds is derived by dividing the latter by the former.

The results of the spectral fit for the H I component are not used to determine  $X_{\text{CO}}$  in the pionic method. The fits to the spectral components shown in Figs. 7a, 8a and 9a are only to check overall consistency of our analyses. Their normalizations are consistent within the uncertainty in the H I column density discussed in Section 4.

### 3.3.2. Spectra obtained with H<sub>2</sub>-template-1

The fitted spectra are plotted as sums of pionic and bremsstrahlung emissions in Fig. 7a, b for the H I spatial template and the H<sub>2</sub>-template-1 (Orion A Region I, II, and Orion B combined), giving  $\chi^2/\text{dof}$  of 17.7/14 and 20.2/14, respectively.

We give the  $X_{\text{CO}}$  value obtained from the fitted pionic spectra in Table 2. Since the fit is substantially poorer than those for H<sub>2</sub>-template-2 and 3 (see Fig. 5), the value should be taken just as a reference value. For this reason we do not quote systematic errors in the table.

### 3.3.3. Spectra obtained with H<sub>2</sub>-template-2

The fitted spectra are plotted as sums of pionic and bremsstrahlung emissions in Fig. 8b, c, d for Orion A Region I, II and Orion B, giving  $\chi^2/\text{dof}$  of 14.0/14, 18.5/14, and 10.6/14, respectively. The  $X_{\text{CO}}$  values obtained for the 4 regions from the fitted pionic spectra are given in Table 2.

The coefficient  $X_{\text{CO}}$  is significantly higher for Orion A Region I than for other regions, consistent with the slopes obtained in Subsection 3.2 in the pixel-by-pixel correlation study. This also can be seen in the  $X_{\text{CO}}$  obtained with the H<sub>2</sub>/H I method.

We note that the fraction of the H I component in the gamma-ray spectrum integrated in the 3 Orion regions is comparable to that associated with  $W_{\text{CO}}$  (see Fig. 10a). This is because the solid angle subtended by the Orion molecular clouds is a small fraction of our 3 Orion regions in solid angle and the overall mass of atomic gas is greater.

### 3.3.4. Spectra obtained with H<sub>2</sub>-template-3

The fitted spectra integrated over the  $W_{\text{CO}}$  and “dark gas” components are shown in Fig. 9b, c. We give  $X_{\text{CO}}$  for the ROI from the fitted pionic spectrum in Table 2.

The  $X_{\text{CO}}$  obtained in fits with the  $W_{\text{CO}}$  can be compared with those obtained in similar

analyses including the “dark gas” template:  $2.0 \times 10^{20}$  (in the local arm),  $1.9 \times 10^{20}$  (the Perseus arm) and  $0.87 \times 10^{20}$  (the Gould Belt) in the same unit as above (Ackermann et al. 2010; Abdo et al. 2010c).

The spectrum associated with the “dark gas” component is similar in shape to that associated with  $W_{\text{CO}}$  but about half as intense (Fig. 10b). The 2 spectral energy densities (SEDs) become comparable in Orion A Region I as seen in Fig. 10c. The “dark gas” dominates over  $W_{\text{CO}}$  in the pixels near the high-longitude end of Orion A and eventually  $W_{\text{CO}}$  diminishes in the pixels beyond them towards higher longitude.

Our  $X_{\text{CO}}$  measurements given in Table 2 can be compared with those determined using the gamma-ray flux from the Orion-Monoceros complex measured with EGRET:  $(1.35 \pm 0.15) \times 10^{20} \text{ cm}^{-2}(\text{K km s}^{-1})^{-1}$  (Digel et al. 1999). We note there were no Galactic CR propagation models such as GALPROP nor CR measurements as precise as are available now:  $X_{\text{CO}}$  was determined by the  $\text{H}_2/\text{H I}$  method and it compares well with the single  $X_{\text{CO}}$  value of  $1.36 \pm 0.02$  obtained with the H2-template-1.

### 3.4. Total masses of Orion A and B

The distance from the Sun to the Orion nebula (M42) inside the Orion A has recently been measured by parallax to be  $389_{-21}^{+24}$  pc (Sandstrom et al. 2007),  $414 \pm 7$  pc (Menten et al. 2007),  $437 \pm 19$  pc (Hirota et al. 2007), and  $419 \pm 6$  pc (Kim et al. 2008). We adopted 400 pc as the distance to the Orion A and B clouds and used the total pionic gamma-ray fluxes obtained above to get the total masses of Orion A and B outside<sup>14</sup>.

Mass estimation using H<sub>2</sub>-template-2:

$$\begin{aligned} M_{\text{A}} &= (74.5 \pm 1.3) \times 10^3 M_{400} \\ M_{\text{B}} &= (33.5 \pm 0.7) \times 10^3 M_{400} \end{aligned}$$

where

$$M_{400} = \left( \frac{d}{400 \text{ pc}} \right)^2 \times M_{\odot}, \quad (2)$$

and  $d$  is the distance to the clouds. We will discuss the systematic uncertainties in the next section.

Mass estimation using H<sub>2</sub>-template-3: Addition of the “dark gas” changes the estimation of the Orion A and B masses by about 10%.

$$M_{\text{A},W_{\text{CO}}} = (55.1 \pm 0.8) \times 10^3 M_{400}$$

---

<sup>14</sup>We note that the spatial extent of Orion B defined here is significantly different from that used in Wilson et al. (2005) because we are unable to separate Orion B from the complex cloud structures behind due to the broad PSF of the LAT.



$$\begin{aligned}
M_{A,\text{Dark}} &= (27.6 \pm 0.7) \times 10^3 M_{400} \\
M_B &= (36.0 \pm 0.5) \times 10^3 M_{400}.
\end{aligned}$$

The total mass of Orion A ( $\equiv M_{A,W_{\text{CO}}} + M_{A,\text{Dark}}$ ) is  $(82.7 \pm 1.1) \times 10^3 M_{400}$ . The Orion A mass has been estimated by Wilson et al. (2005), assuming  $X_{\text{CO}} = 1.8 \times 10^{20} \text{ cm}^{-2} (\text{K km s}^{-1})^{-1}$  (Dame et al. 2001), to be  $M_A = 91.7 \times 10^3 M_{400}$ . The mass has been estimated separately for Orion A Regions 1, 2, 3, and NGC 2149 in Wilson et al. (2005). Our Orion A (Region I and II) includes their Regions 1, 2, and 3 but overlaps only partially with NGC 2149. Considering the breadth of the PSF and the limited statistics of the data, we could not determine how much of NGC 2149 overlaps our Orion Region I. If we assume about one half of NGC 2149 is in our Orion Region I and the systematic error introduced by this ambiguity is half of the NGC 2149 mass estimated by Wilson et al. (2005), the Orion A mass to be compared becomes  $M_A = (86.3 \pm 5.4) \times 10^3 M_{400}$ . The Orion B region is more complex and such a comparison is very difficult.

#### 4. Discussion

Although the Orion clouds lie away from the Galactic Plane and subtend relatively small solid angle, many Galactic and extragalactic sources contribute to the ROI through the large PSF of the *Fermi*-LAT.

We have analyzed the observed data to extract the intensity associated with the molecular clouds, the 3 Orion regions in particular, by using the 3  $\text{H}_2$ -templates made from  $W_{\text{CO}}$  on the 3 different assumptions for each of the 22 energy bins. The ratio of the normalization factors for H I and  $\text{H}_2$ ,  $A_i/2B_i$ , gives the conversion factor of  $W_{\text{CO}}$  to the mass column density,  $X_{\text{CO}}$  (the  $\text{H}_2/\text{H I}$  method). For this, the H I mass column density must be well understood from the radiative transfer of the H I line and the CR spectrum must be constant in the ROI.

In the second method (the pionic method),  $X_{\text{CO}}$  is determined by comparing the observed pionic gamma-ray intensities with those expected from the CR spectrum at the Orion clouds and the pionic gamma-ray production cross-section. For this, we have to know the absolute CR spectrum and flux, the instrument response function (IRF), and the pionic gamma-ray production cross-section, in particular the pionic gamma-ray contribution from metals in CR and ISM.

In the subsections to follow, we evaluate uncertainties and possible systematic errors in the analyses, especially in evaluating  $X_{\text{CO}}$  in the 3 Orion regions. We then summarize the results obtained in this paper and present possible interpretations thereon.

##### 4.1. Possible Systematic Errors in the Analyses

Systematic errors that affect the correlation measurements between gamma-ray intensities and  $W_{\text{CO}}$  are discussed in two categories: the first one applies commonly to the 3 Orion regions and

the second affects the relation differently in the 3 regions.

#### 4.1.1. CR intensity at the Orion clouds

Uncertainty in the fluxes and spectra of CRs, in particular those of protons, can affect in both categories. The Galactic CR protons that produce pions in our energy range remain in our Galaxy longer ( $\sim 5 \times 10^7$  yrs) than electrons ( $\sim 7 \times 10^6$  yrs) (Lee et al. 2011) and their flux variation within the Galaxy is believed to be predicted well by GALPROP. We note that the CR source distribution, the Galaxy size, and the CR diffusion coefficient are the important inputs to GALPROP. Using the CR spectrum measured at the Earth, we have calculated the CR spectrum in the Orion region for the 2 choices of the CR source distributions and the 3 choices of Galactic halo heights (2, 4, and 10 kpc) used in a GALPROP-based study by Lee et al. (2011). The CR spectrum does not change more than  $\sim 2\%$  from the value used here as long as it is constrained to the measurements at the Earth and to reproduce the Galactic diffuse gamma-ray intensities measured by the *Fermi* LAT (see Lee et al. (2011)). We also note that the gamma-ray spectrum from the local H I (typical distance  $< 1$  kpc) is consistent with the CR proton flux being within  $\sim 10\%$  of that at the Earth (Abdo et al. 2009c).

CRs could be accelerated in the clouds and/or prevented from penetrating into their cores by embedded magnetic field. We first note that there are no strong non-thermal X-ray source nor radio SNR found in the clouds (Feigelson et al. 2002, and references therein). Therefore no appreciable CR acceleration is likely to be taking place in the Orion clouds. The good linear correlation between  $W_{\text{CO}}$  and gamma-ray intensity seen in all 3 Orion regions (Fig. 4a) confirms that the CRs effective in producing pions (kinetic energy  $> 1$  GeV) are penetrating well inside the higher-density parts of the clouds.

Based on these observations we assume that the CR flux in the Orion region is 8% lower than that at the Earth with possible systematic error of  $\pm 10\%$  due mostly to disagreement among recent CR measurements at the Earth and solar demodulation uncertainties.

Uncertainty in the CR flux at the Orion clouds contributes directly to the systematic error in the pionic method but indirectly in the  $\text{H}_2/\text{H I}$  method. In the former, the absolute CR intensity is assumed to be known while the CR intensity is assumed to be the same in the local H I region and the molecular clouds in the latter.

#### 4.1.2. Uncertainty in the instrument response functions

The uncertainty in the absolute calibration of the LAT effective area can also introduce error of the first kind. The effective areas were derived based on Monte Carlo studies of the LAT, checked against beam tests at accelerators (Abdo et al. 2009a; Atwood et al. 2009). Comparisons between

flight data and Monte Carlo studies have been made to quantify the systematic uncertainty in the effective area (Abdo et al. 2009b). At present, we estimate this systematic error to be 10% at 100 MeV, 5% at 500 MeV and 20% at 20 GeV.

The systematic error in the absolute energy scale has been estimated as  $+5/-10\%$  (Abdo et al. 2009e). We have refitted  $X_{\text{CO}}$  after artificially shifting the energy scale by  $+5\%$  and by  $-10\%$ : the number of pionic gamma rays changes less than  $+1/-8\%$  for all 3 Orion regions with all 3  $\text{H}_2$  templates. We include this possible error due to the uncertainty in the energy calibration when assessing the overall systematic error.

The pionic method is affected directly by the uncertainty in the instrument response function while the  $\text{H}_2/\text{H I}$  method is insensitive because it affects the denominator and numerator similarly.

#### 4.1.3. Uncertainty in the spin temperature of H I

In converting the observed 21 cm line emission intensity (Kalberla et al. 2005) to the H I column density,  $T_{\text{S}}$  was assumed to be 125 K. The range of  $T_{\text{S}}$  measured in the local H I gas varies broadly between 90 K and 400 K (e.g., Mohan et al. 2004a,b, and references therein) while we have assumed a likely range for our ROI to be between 90 K and 250 K.

We refitted the *Fermi* data in the ROI with these two extreme  $T_{\text{S}}$  values with  $\text{H}_2$ -template 2 and 3. We then calculated  $X_{\text{CO}}$  by dividing  $B_i$  by  $2A_i$  in Eq. (1), or by extracting the pion component in the spectra. The deviations of  $X_{\text{CO}}$  from those obtained with  $T_{\text{S}}$  of 125 K are taken into account in the systematic errors given in Table 2. The large systematic errors for  $X_{\text{CO}}$  on  $B_i/2A_i$  (Column 3) enter via  $2A_i$  which depends on the absolute calibration of the H I gas density or  $T_{\text{S}}$  in the local H I. The pionic method uses the product of the CR intensity and  $pp \rightarrow \gamma$  cross-section in place of  $2A_i$  and is less directly affected by the uncertainty in H I gas density or  $T_{\text{S}}$  of the local H I, although the uncertainties can have a small indirect effect through the overall spatial fitting. This effect is much smaller than the overall systematic error and negligible. We note that there is some discrepancy between the gamma-ray spectra associated with H I in the ROI and the local H I (Abdo et al. 2009c) as seen in Fig. 8.

#### 4.1.4. Effect of overlapping point source candidates

We have not included the 5 sources overlapping with the Orion clouds (Sec. 3.1.4) because they are all classified as “potentially confused with interstellar diffuse emission or perhaps spurious” (Abdo et al. 2010b). To investigate their potential contribution we repeated the analysis including these sources with the fluxes and spectra listed in the First *Fermi* LAT Catalog. The fit with the pionic method gives the following  $X_{\text{CO}}$  in unit of  $\text{cm}^{-2}(\text{K km s}^{-1})^{-1}$ :  $(2.29 \pm 0.05) \times 10^{20}$  for Orion Region I;  $(1.16 \pm 0.05) \times 10^{20}$  for Orion Region II; and  $(1.24 \pm 0.04) \times 10^{20}$  for Orion B. They are 2%,

19%, and 8% less than those obtained without these point source candidates. In the present study, we assume they are artifacts and add +0/−2, +0/−19, and +0/−8% to the overall systematic error in the 3 Orion regions.

#### 4.1.5. Overall error

For the  $H_2/H\text{ I}$  method, the uncertainty in the H I mass density ( $\sim 20\%$ ) due mostly to the uncertainty in  $T_S$  dominates the systematic error. Other contributions include the overlapping “c” sources (+0/−2, +0/−19, and +0/−8%) and variation in the CR intensity within  $\sim 1$  kpc or between H I and the molecular clouds ( $\pm 5\%$ ), making the total systematic errors for the 3 Orion regions to +25/−28, +25/−44, and +25/−33% as given in Column 3 of Table 2.

For the pionic method, the overall systematic error in determining  $X_{CO}$  comes from the uncertainty in the IRF including that due to the energy calibration uncertainty ( $\pm 10\%$ ), unknown contributions of the overlapping sources (+0/−2, +0/−19, and +0/−8%), uncertainty in the CR intensity ( $\pm 10\%$ ), uncertainty in the  $pp$  pion production cross-section ( $\pm 5\%$ ), and uncertainty in the contribution from heavier nuclei ( $\pm 5\%$ ). We conservatively quote the linear sum of these combinations as the possible systematic error for the 3 Orion regions, which are +30/−32, +30/−49, and +30/−38%, as given in Column 5 of Table 2.

The systematic errors that can affect  $X_{CO}$  differently in the 3 Orion regions are variation in the CR intensity within  $\sim 1$  kpc ( $\pm 5\%$ ) and the overlapping sources. The overall error of this kind is conservatively estimated to be the linear sum of the two, +5/−7, +5/−24, and +5/−13%.

## 4.2. Gamma-ray intensity and $E(J - H)$

The line-of-sight visual attenuation,  $A_V$ , are often used as a gas-mass tracer in theory-based studies of the CO fraction in all molecules including carbon and hydrogen (e.g., Burgh et al. 2010; Wolfire et al. 2010; Glover et al. 2010, and references therein). To calibrate crudely our mass column density with  $A_V$  used in these theory-based analyses, we have related the gamma-ray counts on the horizontal axes of Fig. 4 and  $E(J - H)$  in the 3 Orion regions measured by Dobashi (2011). We note that the atomic and molecular components are assumed to be contained within a fixed length (e.g. 20pc) along the line-of-sight in the theory-based analyses while the components are measured as column densities integrated over unknown lengths along the line-of-sight in observations. Moreover  $E(J - H)$  is known to trace the  $H_2$  gas but also pick up some H I gas through dust mixed with it. Hence the cross-calibration works at best crudely and only in the regions of clouds where the  $H_2$  longitudinal distribution is well confined and the  $H_2$  volume density dominates over that of H I. Despite these uncertainties, it is important that our measurements be compared with theory-based analyses.

We found good linear relations for the pixels with high gamma-ray counts ( $> 300$  per  $\text{deg}^2$ ) in all 3 Orion regions and could correlate the gamma-ray count scale on the horizontal axes of Fig. 4 to  $E(J - H)$  assuming  $A_V = R_{V-EJH} \times E(J - H)$ . The  $R_{V-EJH}$  has been determined observationally and its value ranges between 7.8 (Dobashi 2011) to 10.9 (Cardelli et al. 1989). The highest point in our count map is  $\sim 700$  per pixel in Orion A Region II where  $\text{H}_2$  concentration is highest and the corresponding value of  $A_V$  is  $\sim 5$  when averaged over  $1 \times 1 \text{ deg}^2$  pixels for an assumed value of  $R_{V-EJH} = 7.8$ . So  $A_V = 5$  on the horizontal axes of Figs. 5 and 6 in Glover et al. (2010) corresponds crudely to  $\sim 700$  counts per pixel assuming  $\text{H}_2$  is well confined (e.g., to  $\sim 20$  pc) along the line-of-sight.

### 4.3. Summary of the Results

The results obtained in the present work are significant beyond the estimated systematic errors. They are:

1. Linearity holds between mass density associated with the Orion clouds and  $W_{\text{CO}}$ : As discussed in Subsection 3.2 and shown in Fig. 4, our results suggest that CRs penetrate to all translucent part of the clouds. Possible shielding of CRs discussed in Aharonian (2001) does not apply to most parts of the Orion clouds.
2. The  $X_{\text{CO}}$  factors calculated with the pionic method and with the  $\text{H}_2/\text{H I}$  method differ by  $\sim 15\%$  but agree within the estimated systematic error (Table 2). The difference can be explained by uncertainties in the column densities of H I and calculation of gamma-ray emissivity per H I atom.
3. The  $X_{\text{CO}}$  factor obtained with the  $\text{H}_2$ -template-2 is found to be larger by  $\sim 40 - 60\%$  in Orion A Region I than Orion A Region II and Orion B for the two methods. The difference is much larger than the systematic error that can affect the  $X_{\text{CO}}$  factor differently in the 3 Orion regions (Table 2).
4. In the “dark gas” scenario, the added “dark gas” accounts for the majority of the gas not traced by  $W_{\text{CO}}$ . One  $X_{\text{CO}}$  factor can then describe the  $W_{\text{CO}}$ -traced  $\text{H}_2$  distribution in the ROI.

### 4.4. Interpretation of our results on $X_{\text{CO}}$

Historically the relation between  $N(\text{H}_2)$  to  $W_{\text{CO}}$  has been considered to depend on the environment around the molecular cloud. The environmental factors discussed in the literature are:

**Metallicity:** This possibility has been discussed in the literature since the late 1980's (e.g., Elmegreen 1989; Bolatto et al. 1999). According to an empirical formula proposed to relate  $X_{\text{CO}}$  to



[O/H] (Wilson 1995; Arimoto et al. 1996), the metallicity must be  $\sim 2$  times higher in Orion A Region I to account for the observed difference in  $X_{\text{CO}}$  between Region I and II, which is unlikely according to Galactic-scale measurements (e.g. Esteban et al. 2005). We note that metallicity is generally considered to be an important environmental factor influencing the  $\text{H}_2$ -to-H I ratio.

**Overlapping H I clumps:** Compact H I clouds with angular diameters of  $1 - 2$ deg have been found in various Galactic locations (e.g. Braun & Strom 1986; Kavars et al. 2003; Lee et al. 2008). A new reanalysis of the LAB H I survey shows no such concentration detected at the sensitivity level of the present study overlapping with the Orion A and B (Kalberla et al. 2010).

**Low density  $\text{H}_2$  not traced well by  $W_{\text{CO}}$ :** Existence of diffuse  $\text{H}_2$  gas not traced well by  $W_{\text{CO}}$  has been discussed in the literature cited in Section 1 and *Fermi* analyses are bringing the discussion to a quantitative level (Ackermann et al. 2010). We refer to the following recent works on the  $\text{H}_2$  and CO fractions and try to interpret our results:

- Burgh et al. (2010) have studied the fractions based on *Hubble Space Telescope* observations and characterized the  $X_{\text{CO}}$  dependency on  $N(\text{H}_2)$ .
- Wolfire et al. (2010) have studied chemical composition of a model cloud theoretically and found that CO becomes depleted because of photodissociation in the periphery where the gas density decreases.
- Glover et al. (2010) have studied the time-dependent  $\text{H}_2$  and CO fractions in clouds through computer simulations and found  $X_{\text{CO}}$  increases sharply where  $N(\text{H}_2)$  decreases for  $A_V < 3.5$ .

All of the above studies predict that the CO/(total C) fraction drops as the  $\text{H}_2$  column density decreases, as toward the periphery of Orion A and B. However the  $W_{\text{CO}}$ -to- $\text{H}_2$  relation and the abundance of  $\text{H}_2$ -without-CO gas may be more complicated. For example, Ikeda et al. (2002) found that  $N(\text{C I})/N(\text{CO})$  increases to high values along all of the peripheries whereas we find Region I of Orion A to be more abundant in CO-depleted gas than Region II. The prediction that  $X_{\text{CO}}$  increases sharply in regions  $A_V < 3.5$  by Glover et al. (2010) is consistent with our finding that the “dark gas” is concentrated in the high-longitude end of Orion A where  $W_{\text{CO}}$  becomes low.

## 5. Conclusion

We have reported on the first 21 months’ observations of Orion A and B with the *Fermi Gamma-ray Space Telescope* in the energy band between  $\sim 178$  MeV and  $\sim 100$  GeV. We have measured the mass column density distribution within the clouds at the angular scale of the instrument PSF using the  $pp \rightarrow \gamma$  production cross-section accurately calibrated at accelerators as well as using

the gamma-ray emissivity of the local H I gas. We found with the pionic method that a linear relation holds between mass density and  $W_{\text{CO}}$  with  $X_{\text{CO}} = 2.34, 1.43, 1.35 \times 10^{20} \text{ cm}^{-2}(\text{K km s}^{-1})^{-1}$  with a systematic uncertainty of  $+5/-7$ ,  $+5/-24$ , and  $+5/-13\%$  (relative in the 3 regions), and  $+30/-32$ ,  $+30/-49$ , and  $+30/-38\%$  (absolute) for Orion A Region I, Region II, and Orion B, respectively. These values are consistent with the  $X_{\text{CO}}$  values determined with the more traditional  $\text{H}_2/\text{H I}$  method ( $X_{\text{CO}} = 1.97, 1.20, 1.14 \times 10^{20} \text{ cm}^{-2}(\text{K km s}^{-1})^{-1}$ ) within our overall systematic error. This implies that Galactic CRs are penetrating into most parts of the clouds. The analyses also included the “dark gas” (Grenier et al. 2005) not traced by CO or H I. We found that the gamma-ray flux associated with the “dark gas” spatial template exceeds that associated with the  $W_{\text{CO}}$  template in Orion A Region I. The situation is reversed in Region II and in Orion B. This is generally consistent with the fit finding a higher  $X_{\text{CO}}$  value for Orion Region I in the absence of the dark-gas template.

We have interpreted the increase in  $X_{\text{CO}}$  and “dark gas” fraction in Orion A Region I in the light of recent studies of the relation between the  $\text{H}_2$  and CO fractions by Burgh et al. (2010); Wolfire et al. (2010); Glover et al. (2010).  $X_{\text{CO}}$  is expected to increase rapidly as the gas column density decreases to  $A_V \sim 3.5$  or less (Glover et al. 2010). The mass column density we have measured in Region I corresponds to  $A_V < 4$ , close to the predicted threshold for onset of the non-linearity predicted between  $W_{\text{CO}}$  and  $N(\text{H}_2)$ . The mass column density drops further ( $A_V < 2$ ) toward the high Galactic longitude end of the Orion A where the gas becomes “dark” to  $W_{\text{CO}}$ , consistent with the predicted non-linear relation.

The *Fermi*-LAT collaboration is continuing to reduce uncertainty in the IRF, identify extended gamma-ray sources, and improve the modeling of the Galactic-scale diffuse gamma-ray emission. We expect the systematic uncertainties quoted in subsection 4.1 to be reduced significantly through these efforts. The systematic uncertainty in the CR spectra and the H I mass density also will be reduced when the data from new experiments and surveys become available. The present analyses can then be updated to a higher precision and the relation among  $W_{\text{CO}}$  and the gas mass density characterized further for various molecular clouds in the Galaxy.

#### *Acknowledgments*

The *Fermi* LAT Collaboration acknowledges generous ongoing support from a number of agencies and institutes that have supported both the development and the operation of the LAT as well as scientific data analysis. These include the National Aeronautics and Space Administration and the Department of Energy in the United States, the Commissariat à l’Energie Atomique and the Centre National de la Recherche Scientifique / Institut National de Physique Nucléaire et de Physique des Particules in France, the Agenzia Spaziale Italiana and the Istituto Nazionale di Fisica Nucleare in Italy, the Ministry of Education, Culture, Sports, Science and Technology (MEXT), High Energy Accelerator Research Organization (KEK) and Japan Aerospace Exploration Agency (JAXA) in Japan, and the K. A. Wallenberg Foundation, the Swedish Research Council and the Swedish National Space Board in Sweden.

Additional support for science analysis during the operations phase is gratefully acknowledged from the Istituto Nazionale di Astrofisica in Italy and the Centre National d'Études Spatiales in France.

## REFERENCES

- Abdo, A., et al. 2009a, *Astropar. Phys.*, 32, 193
- . 2009b, *ApJ*, 696, 1084
- . 2009c, *ApJ*, 703, 1249
- . 2009d, *ApJS*, 183, 46
- . 2009e, *Phys. Rev. Lett.*, 102, 181101
- . 2009f, *Phys. Rev. Lett.*, 103, 251101
- . 2010a, *Phys. Rev. Lett.*, 104, 101101
- . 2010b, *ApJS*, 188, 405
- . 2010c, *ApJ*, 710, 133
- , 2011, arXiv:1108.1435v1 (to appear in *ApJS*)
- Ackermann, M., et al. 2010, *ApJ*, 726, 81
- Ade, P. A. R., et al. 2011, ArXiv e-prints 1101.2029
- Aharonian, F. A. 2001, *Space Sci. Rev.*, 99, 187
- Arimoto, N., Sofue, Y., & Tsujimoto, T. 1996, *PASJ*, 48, 275
- Atwood, W. B., et al. 2009, *ApJ*, 697, 1071
- Balakrishnan, N., Yan, M., & Dalgarno, A. 2002, *ApJ*, 568, 443
- Bally, J. 2008, in *Handbook of Star Forming Regions: Volume I, The Northern Sky*, ed. B. Reipurth (ASP Conference Series), 459–482
- Beichman, C. A., Neugebauer, G., Habing, H. J., Clegg, P. E., & Chester, T., eds. 1988, *Infrared astronomical satellite (IRAS) catalogs and atlases*. (NASA RP-1190)
- Bell, T. A., Roueff, E., Viti, S., & Williams, D. A. 2006, *MNRAS*, 371, 1865
- Bell, T. A., Viti, S., & Williams, D. A. 2007, *MNRAS*, 378, 983

- Bergin, E. A., & Tafalla, M. 2007, *ARA&A*, 45, 339
- Bertsch, D. L., Dame, T. M., Fichtel, C. E., Hunter, S. D., Sreekumar, P., Stacy, J. G., & Thaddeus, P. 1993, *ApJ*, 416, 587
- Bloemen, J. B. G. M., Caraveo, P. A., Hermsen, W., Lebrun, F., Maddalena, R. J., Strong, A. W., & Thaddeus, P. 1984, *A&A*, 139, 37
- Bolatto, A. D., Jackson, J. M., & Ingalls, J. G. 1999, *ApJ*, 513, 275
- Braun, R., & Strom, R. G. 1986, *A&A*, 164, 193
- Bronfman, L., Cohen, R. S., Alvarez, H., May, J., & Thaddeus, P. 1988, *ApJ*, 324, 248
- Burgh, E. B., France, K., & McCandliss, S. R. 2007, *ApJ*, 658, 446
- Burgh, E. B., France, K., & Jenkins, E. B. 2010, *ApJ*, 708, 334
- Caraveo, P. A., et al. 1980, *A&A*, 91, L3
- Cardelli, J. A., Clayton, G. C., & Mathis, J. S. 1989, *ApJ*, 345, 245
- Cecchi-Pestellini, C., Bodo, E., Balakrishnan, N., & Dalgarno, A. 2002, *ApJ*, 571, 1015
- Dame, T. M., et al. 1987, *ApJ*, 322, 706
- Dame, T. M., Hartmann, D., & Thaddeus, P. 2001, *ApJ*, 547, 792
- Dickman, R. L., Snell, R. L., & Schloerb, F. P. 1986, *ApJ*, 309, 326
- Digel, S. W., Hunter, S. D., & Mukherjee, R. 1995, *ApJ*, 441, 270
- Digel, S. W., Aprile, E., Hunter, S. D., Mukherjee, R., & Xu, F. 1999, *ApJ*, 520, 196
- Dobashi, K., Uehara, H., Kandori, R., Sakurai, T., Kaiden, M., Umemoto, T., & Sato, F. 2005, *PASJ*, 57, S1
- Dobashi, K. 2011 *PASJ*, 63, S1
- Elmegreen, B. G. 1989, *ApJ*, 338, 178
- Esteban, C., García-Rojas, J., Peimbert, M., Peimbert, A., Ruiz, M. T., Rodríguez, M., & Carigi, L. 2005, *ApJ*, 618, L95
- Feigelson, E. D., Broos, P., III, J. A. G., Garmire, G., Hillenbrand, L. A., Pravdo, S. H., Townsley, L., & Tsuboi, Y. 2002, *ApJ*, 574, 258
- Ferrière, K. M. 2001, *Rev. Mod. Phys.*, 73, 1031
- Finkbeiner, D. P. 2003 *ApJS*, 146, 407

- Flower, D. R. 2001, *Journal of Physics B: Atomic, Molecular and Optical Physics*, 34, 2731
- Froebrich, D., & Rowles, J. 2010, *MNRAS*, 406, 1350
- Fukui, Y., et al. 2011, private communication
- Gaisser, T. K., & Schaefer, R. K. 1992, *ApJ*, 394, 174
- Glover, S. C. O., Federrath, C., Mac Low, M.-M., & Klessen, R. S. 2010, *MNRAS*, 404, 2
- Gordon, M. A. 1969, *ApJ*, 158, 479
- Grenier, I. A., Casandjian, J.-M., & Terrier, R. 2005, *Science*, 307, 1292
- Hartmann, L., & Burkert, A. 2007, *ApJ*, 654, 988
- Hartman, R. C., et al. 1999, *ApJ*, 123, 79
- Heiles, C. 1976, *ApJ*, 208, L137
- Hirota, T., et al. 2007, *PASJ*, 59, 897
- Hollenbach, D. J., Takahashi, T., & Tielens, A. G. G. M. 1991, *ApJ*, 377, 192
- Ikedo, M., Oka, T., Tatematsu, K., Sekimoto, Y., & Yamamoto, S. 2002, *ApJ*, 139, 467
- Kalberla, P. M. W., Burton, W. B., Hartmann, D., Arnal, E. M., Bajaja, E., Morras, R., & Pöppel, W. G. L. 2005, *A&A*, 440, 775
- Kalberla, P. M. W., McClure-Griffiths, N. M., Pisano, D. J. and Calabretta, M. R., Alyson Ford, H., Lockman, F. J., Staveley-Smith, L., Kerp, J., Winkel, B., Murphy, T., & Newton-McGee, K. 2010, *A&A*, 521, A17
- Kamae, T., Karlsson, N., Mizuno, T., Abe, T., & Koi, T. 2006, *ApJ*, 647, 692; Erratum Kamae, T., Karlsson, N., Mizuno, T., Abe, T., & Koi, T. 2007, *ApJ*, 662, 779
- Kavars, D. W., Dickey, J. M., McClure-Griffiths, N. M., Gaensler, B. M., & Green, A. J. 2003, *ApJ*, 598, 1048
- Kim, M. K., et al. 2008, *PASJ*, 60, 991
- Kopp, M., Roueff, E., & Pineau des Forêts, G. 2000, *MNRAS*, 315, 37
- Krčo, M., Goldsmith, P. F., Brown, R. L., & Li, D. 2008, *ApJ*, 689, 276
- Kutner, M. L., & Leung, C. M. 1985, *ApJ*, 291, 188
- Lee, J.-J., Koo, B.-C., Yun, M. S., Stanimirović, S., Heiles, C., & Heyer, M. 2008, *The Astronomical Journal*, 135, 796



- Lee, S.-H., et al. 2011, *Astroparticle Phys.* 35, 211
- Liszt, H. S. 2006, *A&A*, 458, 507
- . 2007, *A&A*, 476, 291
- Lombardi, M., & Alves, J. 2001, *A&A*, 377, 1023
- Maddalena, R. J., Morris, M., Moscowitz, J., & Thaddeus, P. 1986, *ApJ*, 303, 375
- Magnani, L., Blitz, L., & Wouterloot, J. G. A. 1988, *ApJ*, 326, 909
- Magnani, L., Chastain, R. J., Kim, H. C., Hartmann, D., Truong, A. T., & Thaddeus, P. 2003, *ApJ*, 586, 1111
- Maloney, P., & Black, J. H. 1988, *ApJ*, 325, 389
- Mengel, M., De Luca, F. C., & Herbst, E. 2001, *Can J. Phys.*, 79, 589
- Menten, K. M., Reid, M. J., Forbrich, J., & Brunthaler, A. 2007, *A&A*, 474, 515
- Mohan, R., Dwarakanath, K., & Srinivasan, G. 2004a, *Journal of Astrophysics and Astronomy*, 25, 143
- . 2004b, *Journal of Astrophysics and Astronomy*, 25, 185
- Mori, M. 2009, *Astropar. Phys.*, 31, 341
- Murthy, J., Sahnou, D. J., & Henry, R. C. 2005, *ApJ*, 618, L99
- O'Dell, C. R. 2001, *ARA&A*, 39, 99
- Orlando, E. & Strong, A. W., 2008, In *Proceedings of the 30th International Cosmic Ray Conference*, 505
- Porter, T. A., Moskalenko, I. V., Strong, A. W., Orlando, E., & Bouchet, L. 2008, *ApJ*, 682, 400
- Prisinzano, L., et al. 2008, *ApJ*, 677, 401
- Reynolds, R. J., & Ogden, P. M. 1979, *ApJ*, 229, 942
- Rowles, J., & Froebrich, D. 2009, *MNRAS*, 395, 1640
- Sanders, D. B., Solomon, P. M., & Scoville, N. Z. 1984, *Astrophys. Jour.*, 276, 182
- Sandstrom, K. M., Peek, J. E. G., Bower, G. C., Bolatto, A. D., & Plambeck, R. L. 2007, *ApJ*, 667, 1161
- Schlegel, D. J., Finkbeiner, D. P., & Davis, M. 1998, *ApJ*, 500, 525

- Sheffer, Y., Rogers, M., Federman, S. R., Abel, N. P., Gredel, R., Lambert, D. L., & Shaw, G. 2008, *ApJ*, 687, 1075
- Shepler, B. C., et al. 2007, *A&A*, 475, L15
- Snow, T. P., & McCall, B. J. 2006, *Ann. Rev. A&A*, 44, 367
- Strong, A. W., et al. 1988, *A&A*, 207, 1
- Strong, A. W., & Moskalenko, I. V. 1998, *ApJ*, 509, 212
- Strong, A. W., Moskalenko, I. V., & Reimer, O. 2000, *ApJ*, 537, 763
- Taylor, S. D., Hartquist, T. W., & Williams, D. A. 1993, *MNRAS*, 264, 929
- van Dishoeck, E. F., & Black, J. H. 1986, *ApJS*, 62, 109
- van Dishoeck, E. F., & Black, J. H. 1988, *ApJ*, 334, 771
- Wall, W. F. 2007, *MNRAS*, 375, 278
- Wernli, M., Valiron, P., Faure, A., Wiesenfeld, L., Jankowski, P., & Szalewicz, K. 2006, *A&A*, 446, 367
- Wilson, C. D. 1995, *ApJ*, 448, L97
- Wilson, B. A., Dame, T. M., Mashedier, M. R. W., & Thaddeus, P. 2005, *A&A*, 430, 523
- Wolfire, M. G., Hollenbach, D., & McKee, C. F. 2010, *ApJ*, 716, 1191

Table 1. Gamma-ray emissivity fitted with H<sub>2</sub>-template-2

Energy Range (MeV)	Emissivity per H <sup>a</sup>	Emissivity per W <sub>CO</sub> <sup>b</sup>	
		Orion Region I	Orion Region II
178 - 237	(4.81 ± 0.26) × 10 <sup>-29</sup>	(1.04 ± 0.08) × 10 <sup>-28</sup>	(5.20 ± 0.84) × 10 <sup>-29</sup>
237 - 316	(3.15 ± 0.10) × 10 <sup>-29</sup>	(6.36 ± 0.39) × 10 <sup>-29</sup>	(3.50 ± 0.37) × 10 <sup>-29</sup>
316 - 422	(1.81 ± 0.04) × 10 <sup>-29</sup>	(3.08 ± 0.21) × 10 <sup>-29</sup>	(2.16 ± 0.18) × 10 <sup>-29</sup>
422 - 562	(1.05 ± 0.02) × 10 <sup>-29</sup>	(1.95 ± 0.11) × 10 <sup>-29</sup>	(1.24 ± 0.09) × 10 <sup>-29</sup>
562 - 750	(5.72 ± 0.12) × 10 <sup>-30</sup>	(1.29 ± 0.07) × 10 <sup>-29</sup>	(6.15 ± 0.46) × 10 <sup>-30</sup>
750 - 1000	(3.20 ± 0.08) × 10 <sup>-30</sup>	(5.97 ± 0.37) × 10 <sup>-30</sup>	(4.08 ± 0.27) × 10 <sup>-30</sup>
1000 - 1334	(1.69 ± 0.09) × 10 <sup>-30</sup>	(3.16 ± 0.23) × 10 <sup>-30</sup>	(2.08 ± 0.15) × 10 <sup>-30</sup>
1334 - 1778	(6.75 ± 0.30) × 10 <sup>-31</sup>	(1.55 ± 0.13) × 10 <sup>-29</sup>	(1.06 ± 0.08) × 10 <sup>-30</sup>
1778 - 2371	(4.19 ± 0.25) × 10 <sup>-31</sup>	(7.48 ± 0.77) × 10 <sup>-31</sup>	(6.08 ± 0.53) × 10 <sup>-31</sup>
2371 - 3162	(1.83 ± 0.14) × 10 <sup>-31</sup>	(4.01 ± 0.47) × 10 <sup>-31</sup>	(2.60 ± 0.29) × 10 <sup>-31</sup>
3162 - 4217	(7.97 ± 2.72) × 10 <sup>-32</sup>	(2.16 ± 0.29) × 10 <sup>-31</sup>	(1.23 ± 0.17) × 10 <sup>-31</sup>
4217 - 5623	(4.07 ± 0.29) × 10 <sup>-32</sup>	(6.98 ± 1.46) × 10 <sup>-32</sup>	(4.77 ± 0.95) × 10 <sup>-32</sup>
5623 - 10000	(1.19 ± 0.38) × 10 <sup>-32</sup>	(2.27 ± 0.47) × 10 <sup>-32</sup>	(1.05 ± 0.27) × 10 <sup>-32</sup>
10000 - 23714	(1.42 ± 1.01) × 10 <sup>-33</sup>	(2.12 ± 0.95) × 10 <sup>-33</sup>	(1.48 ± 0.53) × 10 <sup>-33</sup>
23714 - 100000	(4.16 ± 3.06) × 10 <sup>-35</sup>	(1.07 ± 0.79) × 10 <sup>-34</sup>	(1.57 ± 3.34) × 10 <sup>-34</sup>
			(6.17 ± 0.52) × 10 <sup>-29</sup>
			(3.64 ± 0.26) × 10 <sup>-29</sup>
			(2.32 ± 0.13) × 10 <sup>-29</sup>
			(1.17 ± 0.07) × 10 <sup>-29</sup>
			(6.96 ± 0.41) × 10 <sup>-30</sup>
			(3.50 ± 0.24) × 10 <sup>-30</sup>
			(1.70 ± 0.14) × 10 <sup>-30</sup>
			(8.71 ± 0.80) × 10 <sup>-31</sup>
			(4.82 ± 0.49) × 10 <sup>-31</sup>
			(1.92 ± 0.27) × 10 <sup>-31</sup>
			(9.34 ± 1.56) × 10 <sup>-32</sup>
			(4.33 ± 0.90) × 10 <sup>-32</sup>
			(1.10 ± 0.26) × 10 <sup>-32</sup>
			(1.61 ± 0.59) × 10 <sup>-33</sup>
			(1.14 ± 0.53) × 10 <sup>-34</sup>

Note. — Errors are statistical only

<sup>a</sup>MeV<sup>-1</sup>s<sup>-1</sup>sr<sup>-1</sup> per H atom

<sup>b</sup>MeV<sup>-1</sup>s<sup>-1</sup>sr<sup>-1</sup>(2 × 10<sup>20</sup>cm<sup>-2</sup>(K km s<sup>-1</sup>)<sup>-1</sup>)<sup>-1</sup>

Table 2.  $X_{\text{CO}}$  obtained on H<sub>2</sub>-template-1, 2, and 3

Region	$X_{\text{CO}}^a$ on $B/2A$	Sys. error <sup>b</sup> (%)	$X_{\text{CO}}^a$ on pion	Sys. error <sup>c</sup> (%)
H <sub>2</sub> -template-1				
Entire ROI	$1.36 \pm 0.02_{\text{stat}}$	NA	$1.63 \pm 0.02_{\text{stat}}$	NA
H <sub>2</sub> -template-2				
Orion A Region I	$1.97 \pm 0.05_{\text{stat}}$	+25/ - 28	$2.34 \pm 0.05_{\text{stat}}$	+30/ - 32
Orion A Region II	$1.20 \pm 0.03_{\text{stat}}$	+25/ - 44	$1.43 \pm 0.04_{\text{stat}}$	+30/ - 49
Orion B	$1.14 \pm 0.03_{\text{stat}}$	+25/ - 33	$1.35 \pm 0.03_{\text{stat}}$	+30/ - 38
Elsewhere	$1.43 \pm 0.04_{\text{stat}}$	NA <sup>c</sup>	$1.69 \pm 0.04_{\text{stat}}$	NA <sup>d</sup>
H <sub>2</sub> -template-3				
Entire ROI	$1.21 \pm 0.02_{\text{stat}}$	+25/ - 37% <sup>e</sup>	$1.32 \pm 0.02_{\text{stat}}$	+30/ - 40 <sup>e</sup>

<sup>a</sup>In unit of  $10^{20} \text{ cm}^{-2}(\text{K km s}^{-1})^{-1}$ .

<sup>b</sup>The systematic error is discussed in Subsection 4.1: it comes from a combination of uncertainties in the H I spin temperature and in the fitting process. The systematic errors which may apply differently to the 3 Orion regions are +5/ - 8, +5/ - 24, and +5/ - 13%, respectively.

<sup>c</sup>The systematic error is discussed in Subsection 4.1. The systematic errors are the same as b.

<sup>d</sup>We have not attempted to estimate systematic error outside of the Orion regions in this study.

<sup>e</sup>The average of the systematic errors estimated for the 3 Orion regions.

Table 3. Gamma-ray emissivity fitted with H<sub>2</sub>-template-3

Energy Range (MeV)	Emissivity per H atom <sup>a</sup>	Emissivity per $W_{CO}$ <sup>b</sup>	Emissivity per $E(B-V)_{res}$ <sup>c</sup>
178 – 237	$(4.51 \pm 0.08) \times 10^{-29}$	$(5.56 \pm 0.31) \times 10^{-29}$	$(1.00 \pm 0.10) \times 10^{-27}$
237 – 316	$(2.99 \pm 0.08) \times 10^{-29}$	$(3.39 \pm 0.27) \times 10^{-29}$	$(5.60 \pm 0.83) \times 10^{-28}$
316 – 422	$(1.68 \pm 0.07) \times 10^{-29}$	$(2.03 \pm 0.11) \times 10^{-29}$	$(3.95 \pm 0.36) \times 10^{-28}$
422 – 562	$(1.02 \pm 0.08) \times 10^{-29}$	$(1.13 \pm 0.05) \times 10^{-29}$	$(2.07 \pm 0.16) \times 10^{-28}$
562 – 750	$(5.39 \pm 0.08) \times 10^{-30}$	$(6.51 \pm 0.21) \times 10^{-30}$	$(1.37 \pm 0.09) \times 10^{-28}$
750 – 1000	$(2.97 \pm 0.09) \times 10^{-30}$	$(3.54 \pm 0.16) \times 10^{-30}$	$(5.57 \pm 0.60) \times 10^{-29}$
1000 – 1334	$(1.58 \pm 0.05) \times 10^{-30}$	$(1.86 \pm 0.09) \times 10^{-30}$	$(3.57 \pm 0.35) \times 10^{-29}$
1334 – 1778	$(8.00 \pm 1.02) \times 10^{-31}$	$(9.37 \pm 0.43) \times 10^{-31}$	$(1.86 \pm 0.16) \times 10^{-29}$
1778 – 2371	$(3.64 \pm 0.25) \times 10^{-31}$	$(5.00 \pm 0.31) \times 10^{-31}$	$(7.45 \pm 1.19) \times 10^{-30}$
2371 – 3162	$(1.51 \pm 0.14) \times 10^{-31}$	$(2.19 \pm 0.17) \times 10^{-31}$	$(4.82 \pm 0.68) \times 10^{-30}$
3162 – 4217	$(6.56 \pm 0.89) \times 10^{-32}$	$(1.06 \pm 0.10) \times 10^{-31}$	$(2.18 \pm 0.40) \times 10^{-30}$
4217 – 5623	$(3.82 \pm 1.71) \times 10^{-32}$	$(4.31 \pm 0.49) \times 10^{-32}$	$(6.50 \pm 2.34) \times 10^{-31}$
5623 – 10000	$(1.06 \pm 0.14) \times 10^{-32}$	$(1.07 \pm 0.16) \times 10^{-32}$	$(2.20 \pm 0.68) \times 10^{-31}$
10000 – 23714	$(1.35 \pm 0.15) \times 10^{-33}$	$(1.68 \pm 0.24) \times 10^{-33}$	$(1.72 \pm 0.92) \times 10^{-32}$
23714 – 100000	$(4.62 \pm 6.52) \times 10^{-35}$	$(9.55 \pm 3.50) \times 10^{-35}$	$(1.46 \pm 1.22) \times 10^{-33}$

Note. — Errors are statistical only

<sup>a</sup>MeV<sup>-1</sup>s<sup>-1</sup>sr<sup>-1</sup> per H atom

<sup>b</sup>MeV<sup>-1</sup>s<sup>-1</sup>sr<sup>-1</sup>( $2 \times 10^{20}$ cm<sup>-2</sup>(K km s<sup>-1</sup>)<sup>-1</sup>)<sup>-1</sup>

<sup>c</sup>MeV<sup>-1</sup>s<sup>-1</sup>sr<sup>-1</sup>( $2 \times 10^{20}$ mag)<sup>-1</sup>



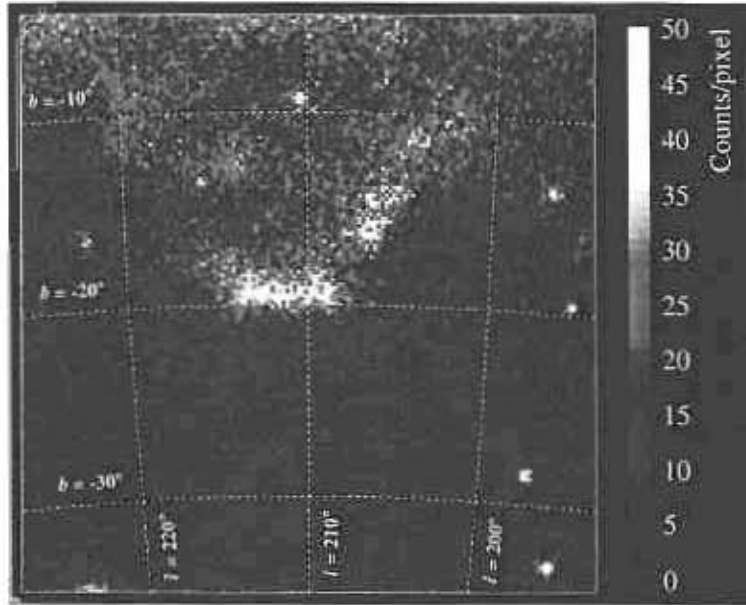


Fig. 1.— Gamma-ray count distribution in the Orion region in the energy band between 178 MeV and 100 GeV in the Hammer-Aitoff projection on the Galactic coordinates. The pixel size is  $0.2 \times 0.2 \text{ deg}^2$ .

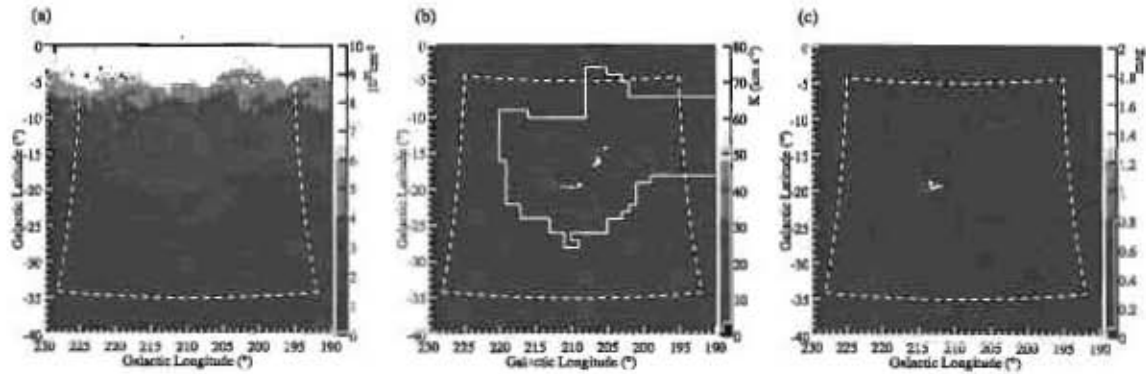


Fig. 2.— (a)  $N(\text{H I})$  template summed over the line-of-sight velocity. The pixel size is  $0.5^\circ \times 0.5^\circ$ . The dashed lines show the boundary of the ROI. (b)  $W_{\text{CO}}$  template used in  $\text{H}_2$ -template-1 and  $\text{H}_2$ -template-2. We used NANTEN data (Fukui et al. 2011) in the area bounded by the solid lines and those by Dame et al. (2001) elsewhere. Pixel resolution is  $0.125^\circ \times 0.125^\circ$ . (c)  $E(B - V)_{\text{res}}$  template used in  $\text{H}_2$ -template-3. Pixel resolution is  $0.5^\circ \times 0.5^\circ$ .

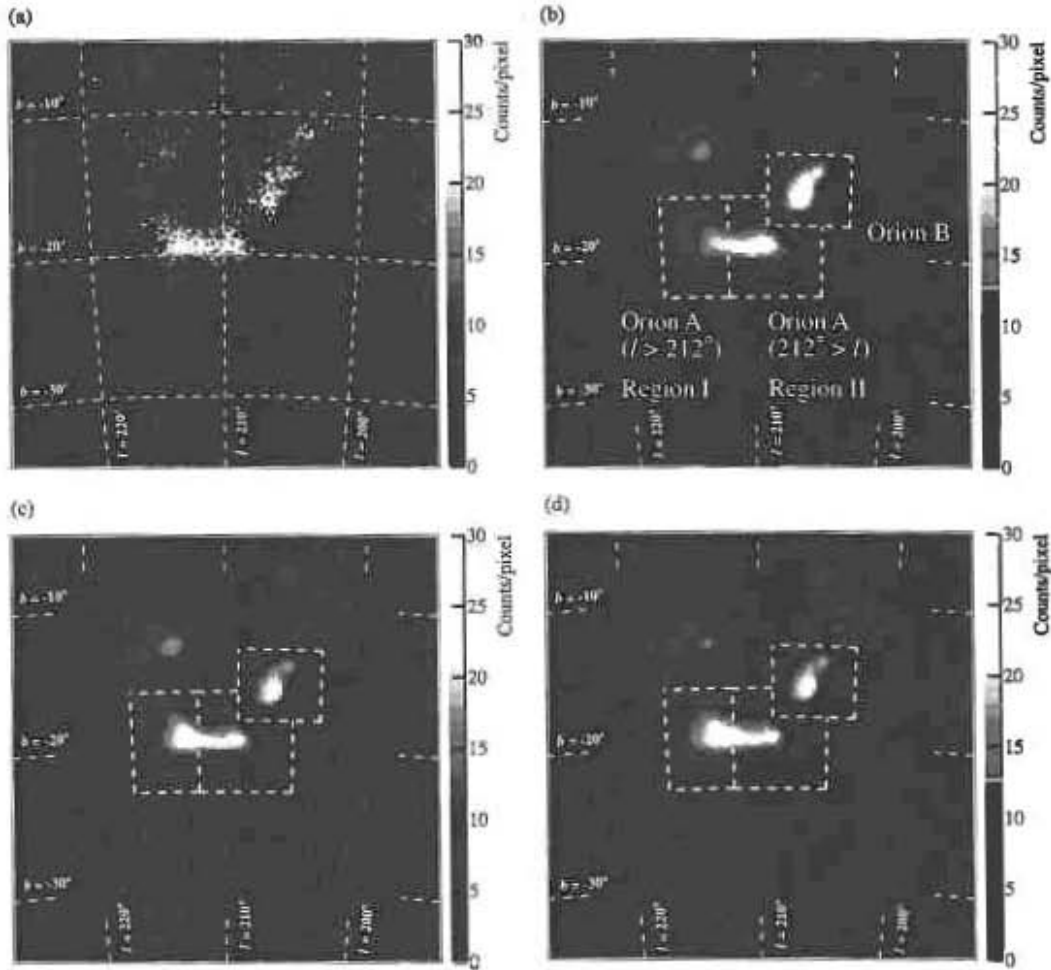


Fig. 3.— (a) Gamma-ray count distribution in the ROI after subtracting the fitted “background” that is the sum of the H I, IC, point-source, and isotropic components. (b) The fitted model map obtained by assuming one common  $X_{\text{CO}}$  for the ROI ( $\text{H}_2$ -template-1). Dashed lines define the boundaries of the 3 Orion regions, Orion A Region I, Region II and Orion B. (c) Same as (b) but obtained by assuming 4 different  $X_{\text{CO}}$  for Orion A Region I, Region II, Orion B, and elsewhere ( $\text{H}_2$ -template-2). (d) Same as (b) but obtained by adding  $E(B - V)_{\text{res}}$  to  $\text{H}_2$ -template-1 ( $\text{H}_2$ -template-3).

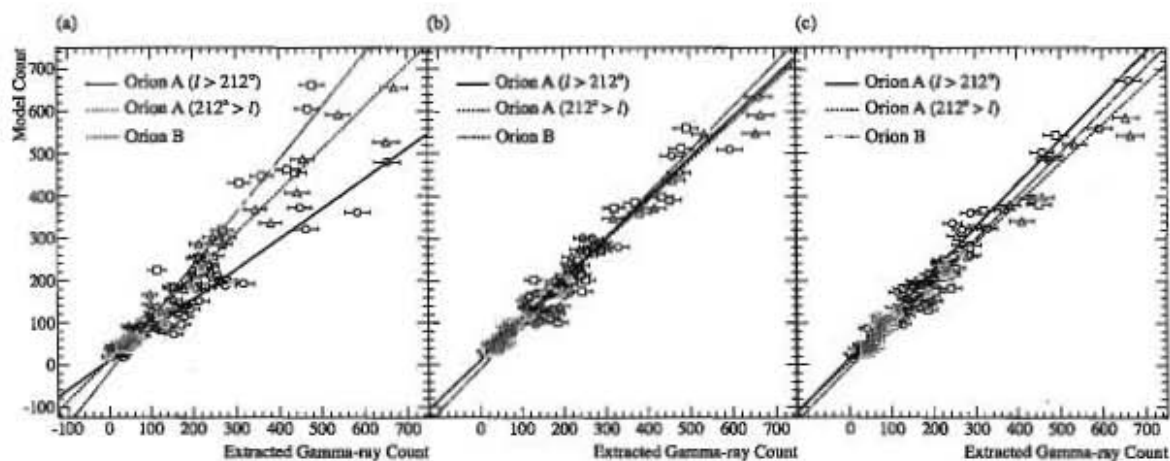


Fig. 4.— (a) Correlation between the gamma-ray count distribution shown in Fig. 3a (the horizontal axis) and that fitted with  $H_2$ -template-1 in Fig. 3b (the vertical axis) for all pixels in the 3 Orion regions. Points represent pixels in Orion A Region I (black circles), Region II (red triangle), and Orion B (blue squares) with fitted lines black, red, and blue, respectively. Error bars represent statistical errors in counts in pixels. Same after replacing the vertical axis for that fitted with  $H_2$ -template-2 (b) and for that fitted with  $H_2$ -template-3 (the sum of  $W_{CO}$  and  $E(B - V)_{res}$  components) (c).

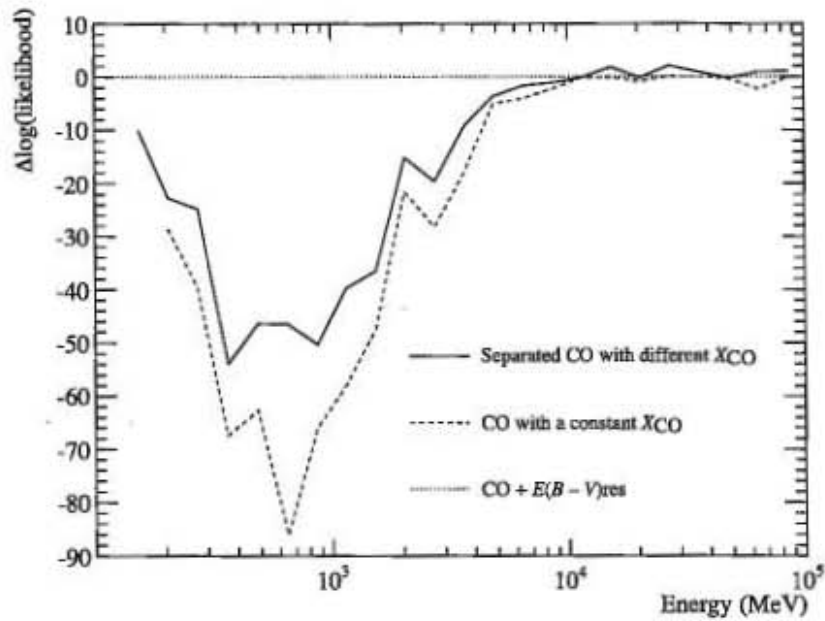


Fig. 5.— Difference in  $\log(\text{Likelihood})$  between the spatial fit using  $\text{H}_2$ -template-3 (dotted line) and either that with  $\text{H}_2$ -template-1 (dashed line) or that with  $\text{H}_2$ -template-2 (solid line) in the ROI for the 22 energy bins. Note that the lines are drawn between the data points only to guide the eye.

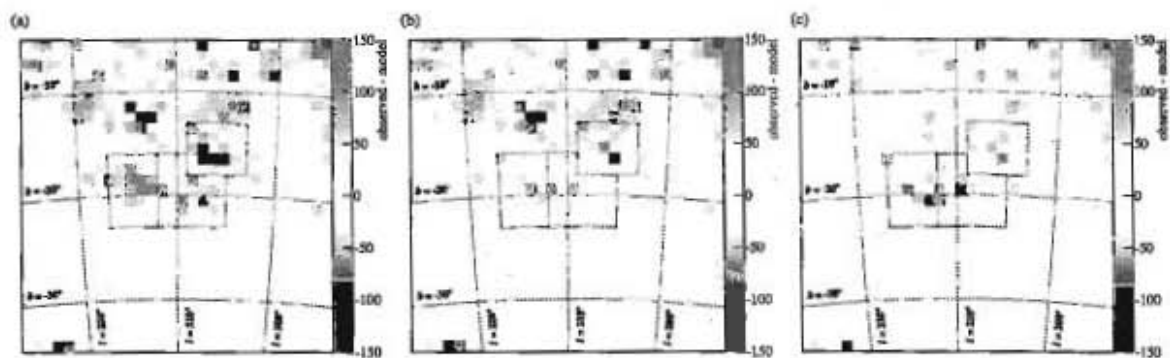


Fig. 6.— Residue in the energy-summed gamma-ray counts of the spatial fit with  $\text{H}_2$ -template-1 (a),  $\text{H}_2$ -template-2 (b), and  $\text{H}_2$ -template-3 (c), binned in  $1 \times 1 \text{ deg}^2$  pixels. The black dotted lines show the boundaries of the 3 regions, Orion A Region I, II, and Orion B.

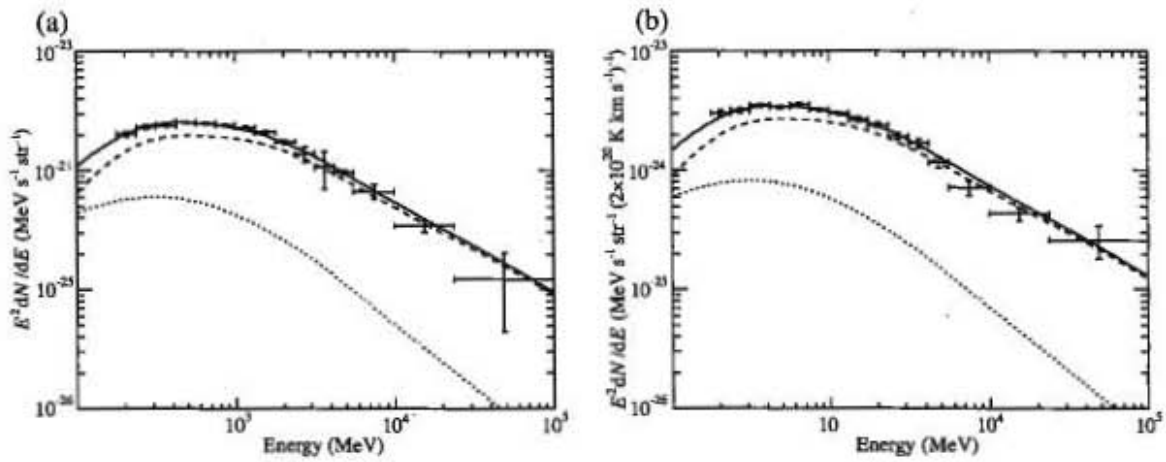


Fig. 7.— Spectral energy densities (SED) associated with local H I ( $T_g = 125$  K assumed) (a) and that associated with H<sub>2</sub>-template-1 (b). The lines are: total (solid), bremsstrahlung (dotted) and pion decay (dashed). The CR spectral shape and electron-to-proton ratio at the Orion clouds were fixed to those used by GALPROP. The vertical axes are normalized to the column density of H I in unit of  $1 \text{ cm}^{-2}$  for (a) and to  $2 \times X_{\text{CO}}$  in unit of  $10^{20} \text{ cm}^{-2} (\text{K km s}^{-1})^{-1}$  for (b). The energy bins between No.13 and No.22 are combined to wider energy bins. Vertical bars represent statistical errors. Note that the spectral fit to H I is not used in evaluating  $X_{\text{CO}}$ .



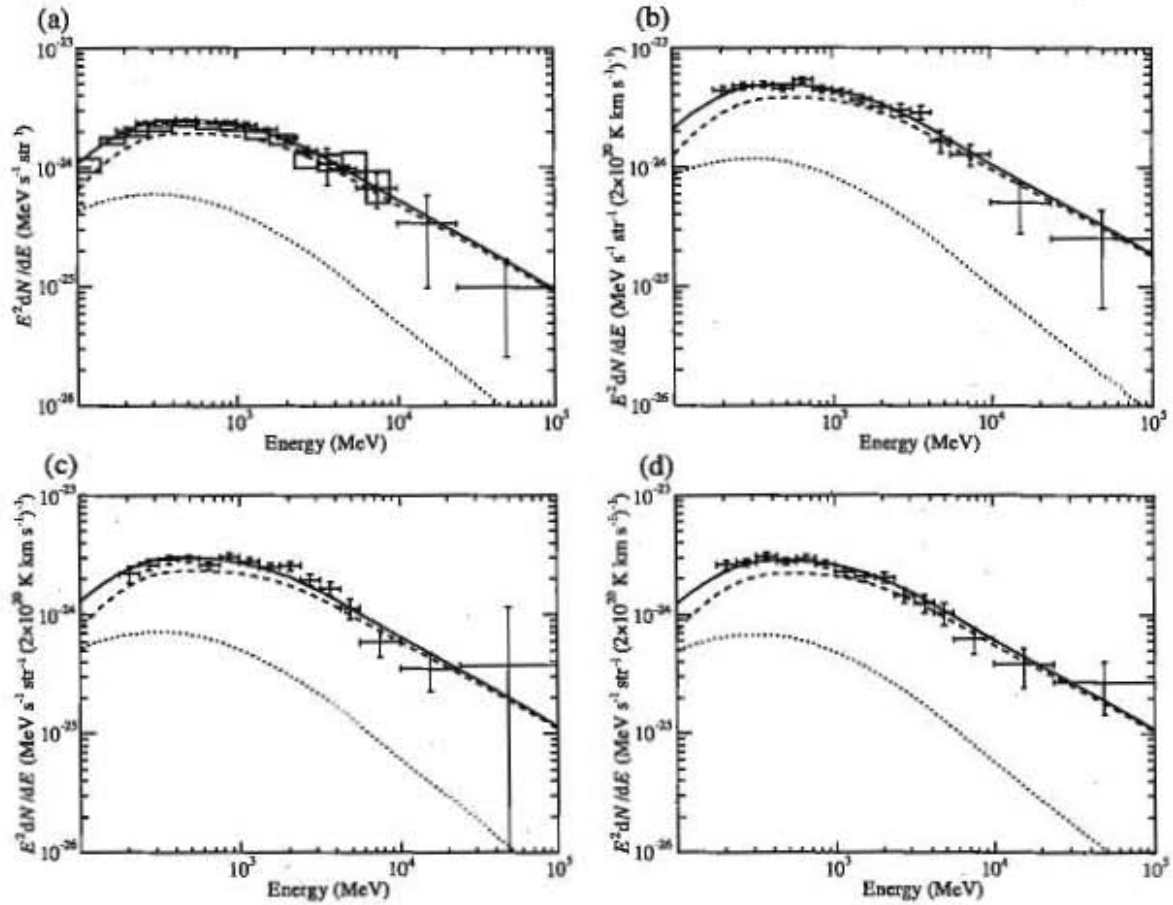


Fig. 8.— Spectral energy density (SED) associated with local H I ( $T_S = 125$  K assumed) (a), Orion A Region I (b), Region II (c), and Orion B (d) for the fit with  $H_2$ -template-2. The corresponding SED obtained for the local H I (Abdo et al. 2009c) is shown by gray squares in (a). The assumption about the CR, the line legends, and the vertical axis units are the same as in Fig. 7.

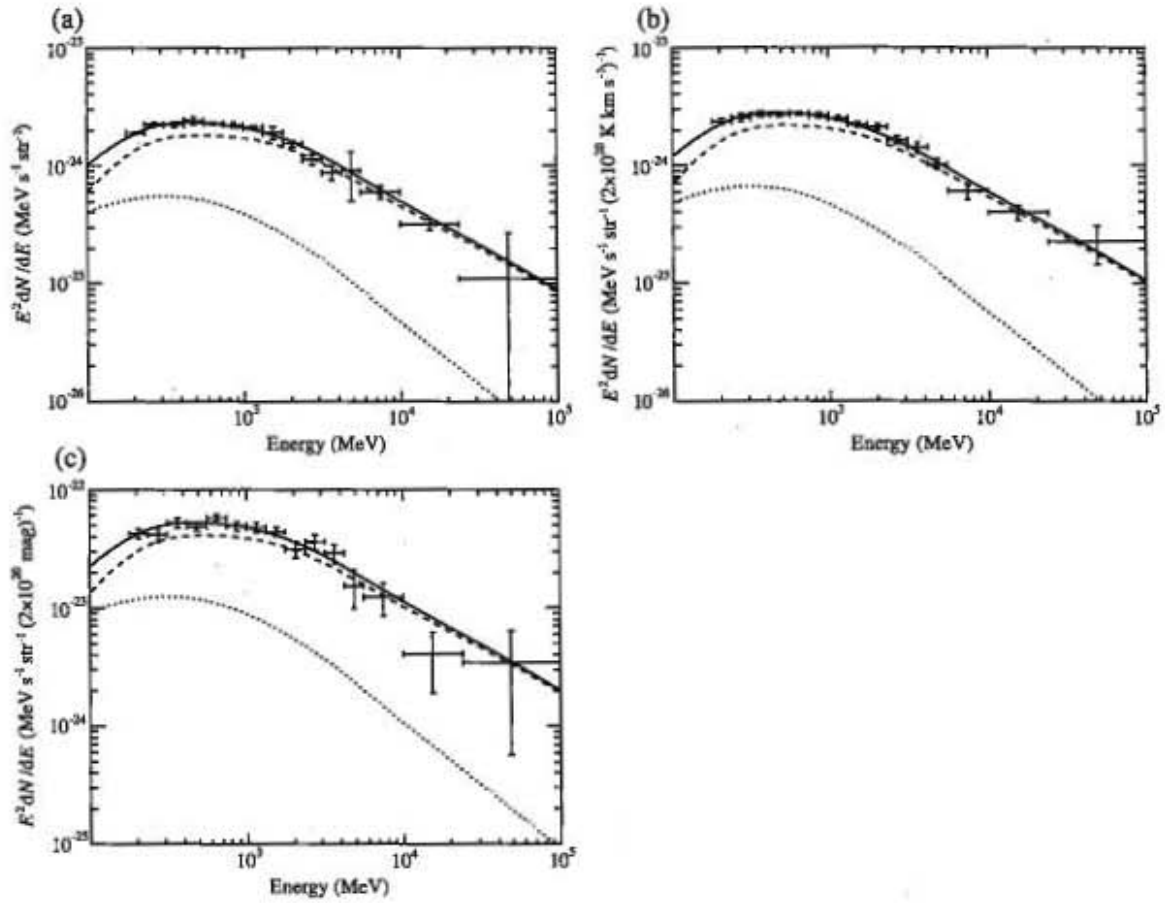


Fig. 9.— SED associated with local H I ( $T_S = 125$  K assumed) (a), that associated with  $W_{CO}$  (b), and that associated with  $E(B - V)_{res}$  (c) obtained with  $H_2$ -template-3. The line legends and vertical axis units are the same as in Fig. 7.

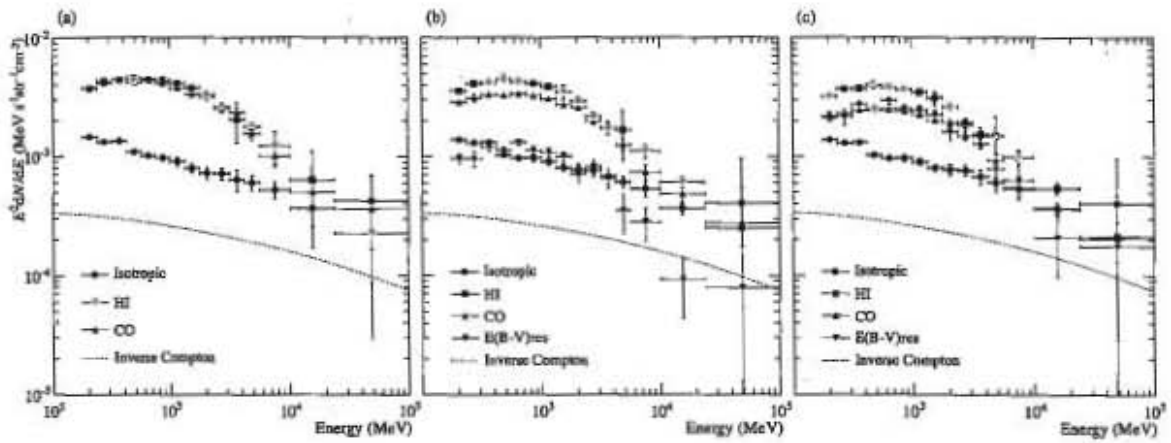


Fig. 10.— Gamma-ray spectra spatially associated with two  $H_2$  templates in the 3 Orion regions marked in Fig. 3b: (a) the sum of the 3 regions obtained with  $H_2$ -template-2; (b) the sum of the 3 regions with  $H_2$ -template-3; (c) Orion A Region I obtained with  $H_2$ -template-3. Black circles show the isotropic component, red squares HI, green upward triangles CO, and purple dashed line the inverse Compton. Blue downward triangles in (b) and (c) represent the spectra associated with  $E(B - V)_{res}$ .

